Mantle-melt partitioning of the highly siderophile elements: new results and application to Mars

K. Righter[1], R. Rowland, II [2], L.R. Danielson[2], M. Humayun[3], S. Yang[3], N. Mayer (Waeselmann)[3,*], and K. Pando [4]

[1] NASA Johnson Space Center, Mailcode XI2, 2101 NASA Parkway, Houston, TX 77058.

[2]Los Alamos National Laboratory, Mail Stop P952, Los Alamos, NM 87545

[3] National High Magnetic Field Laboratory, and Dept. of Earth, Ocean & Atmospheric Science, Florida State Univ., Tallahassee, FL 32310, USA.

[4]Jacobs, NASA Johnson Space Center, Houston, TX 77058,

[*]Present address: University of Hamburg, Hamburg, Germany.

Submitted to *Meteoritics and Planetary Science*, 5/21/2020

Revised October 2020

Abstract - Trace elements and extant and extinct isotopic attributes in martian meteorites have been used to argue that Mars accreted quickly, differentiated into core and mantle, and established several mantle reservoirs, possibly within 10 Ma of T_0. The partitioning of trace elements in the deep mantle has been relatively unstudied, despite the need for such knowledge in understanding magma ocean crystallization and the origin of depleted and enriched mantle reservoirs. The siderophile element composition of the martian

mantle, and lithophile isotopic systems such as Sr, Hf, and Nd, are thought to record evidence for early metal-silicate equilibrium and deep magma ocean at an intermediate depth and pressure of 800 km or 14 GPa. We have carried out experiments across this pressure range to better understand the mineral/melt partitioning of a wide range of elements. These new data are used to evaluate differentiation models for Mars and to help interpret the available isotopic data. The relatively incompatible nature of Re compared to mildly compatible Os means that the crystallization of a deep magma ocean will lead to residual liquids with super chondritic Re/Os, and solids with sub-chondritic Re/Os. Such material available in the mantle could be the source of enriched isotopic reservoir that produced shergottites with + γOs values. On the other hand, slightly sub-chondritic Re/Os ratios in the crystallizing solids would provide a reservoir that could produce - γOs values. Melting of mixtures of these two enriched and depleted end members could explain the Nd-Os isotopic correlations and systematics of shergottites.

Introduction

Highly and moderately siderophile elements (HSE and MSE, respectively) and Os isotopes are used to constrain processes such as accretion, mantle differentiation, crustal recycling, and core-mantle mixing, and the timing and depth of differentiation of Mars (Walker, 2009; Righter et al., 2015). Righter et al. (2015), Righter and Chabot (2011), Brennan et al. (2020), Rai and van Westrenen, 2014), and Yang et al. (2015) showed that the MSE, HSE and volatile contents of the martian mantle (Brandon et al., 2012; Yang et al., 2015) could have been established by deep metal-silicate equilibrium in early Mars (**Figure 1**). Lithophile trace elements and isotopic systems (Rb-Sr, Sm-Nd, Lu-Hf; Debaille et al., 2008), moderately volatile, and weakly siderophile elements (MSE, VSE, WSE, respectively; Righter and Drake, 1996; Righter and Chabot, 2011; Rai and van Westrenen, 2013; Yang et al., 2015; Righter et al., 2015; 2019), and Hf-W isotopes (Kleine et al., 2004) have been used to demonstrate that Mars may have experienced a deep magma ocean in its early history at a depth corresponding to near 14 GPa and temperature of 2400 K.

While the broadly chondritic HSE and S contents of the martian mantle are primarily due to metal-silicate partitioning (Righter et al., 2009, 2015), there are nonetheless portions of the martian mantle with sub-chondritic and super-chondritic ratios of the HSE (Re/Os) and Os isotopes (Tait and Day, 2018; Day et al., 2016; Brandon et al., 2012). Because core formation cannot produce both super- and sub-chondritic mantle reservoirs, it is possible that silicate fractionation has also contributed to establishing the major martian mantle HSE and Os isotopic reservoirs. Thus, HSE patterns for the martian mantle, whether evaluated by element correlations in martian mantle melts (Tait and Day,

2018) or by metal-silicate partitioning calculations, must be explained by a combination of realistic core formation and differentiation processes.

The depleted, intermediate, and enriched shergottites exhibit distinct ranges with respect to Os, Sr, Nd, Hf, and W isotopes (e.g., **Figure 2**) that are thought to result from ancient silicate fractionation within a magma ocean. The enriched and depleted end members may represent mixtures of cumulates and residual liquids established within 10-30 Ma of accretion, as suggested from studies of Sr-Nd-Hf isotopes (Elkins-Tanton, 2003, 2005a,b; Debaille et al., 2007, 2008). Production of the enriched end member by mixing of trapped melt and depleted cumulates should produce a range of IHSE/CHSE ratios (where incompatible HSE or IHSE = Re, Pd, Pt, Au, and compatible HSE or CHSE = Ir, Ru, Os). The role of melts in fractionating Re and Os is well known (Righter et al., 2008a; Day et al., 2016), and the Re/Os ratio of mixtures of melt and deep mantle cumulate phases should also be variable. However, at the PT conditions proposed for the base of the magma ocean for which mineral/melt partitioning of HSE have not yet been measured, the deep mantle minerals majoritic garnet and wadsleyite are stable (Bertka and Fei, 1998),. The role of a cooling magma ocean and associated crystallization in fractionating the HSEs is thus unclear, and models for shallow versus deeper magma ocean crystallization have not been evaluated for Os isotopes. Early silicate and oxide fractionation in a magma ocean setting might be an important secondary process and needs to be quantified.

In addition to mineralogical transitions in the mantle, there might be intra-mantle or intra-reservoir fractionations. For example, as the magma ocean crystallized there could have been garnet- or olivine-rich layers that later became gravitationally unstable leading

to mixing of cumulates and trapped melt within the mantle (Parmentier and Zuber, 2007; Elkins-Tanton et al., 2003). Because of its multitude of crystal lattice sites and compatibility of many trace elements, garnet can play an important role in controlling trace element concentrations in planetary mantle reservoirs and thus producing elemental fractionation (e.g., van Westrenen and Draper, 2007). Furthermore, evidence is building for multiple mantle reservoirs based on water (D/H) and Pb (Barnes et al., 2020; Moriwaki et al., 2020), and mantle heterogeneity in general (Marchi et al., 2020; Brasser and Mojzsis, 2017).

Testing magma ocean crystallization models for a multi-element system including Os isotopes has been hindered by a dearth of partitioning data for the HSE, especially for phases such as deep mantle garnet, ringwoodite and wadsleyite that may be present in the martian mantle at conditions proposed by Debaille et al. (2008). To build on our and others' initial findings for HSE partitioning on low pressure (shallow melting) phases (Righter et al., 2004; Brenan et al., 2003, 2005; Sharp et al., 2015; Malavergne et al., 2016), we examine HSE partitioning at higher PT conditions and search for potential deep mantle host phases for Re, Pt and Os. We begin to examine the partitioning behavior of HSEs between these deep mantle phases with a study of partitioning between majorite garnet (gt), olivine (oliv), wadsleyite (wads), and silicate liquid (melt). The new partition coefficient data are then utilized to test models of mineral-melt fractionation of HSE during the magma ocean stage.

Experimental methodology

A silicate composition that represents the Martian mantle was chosen after Wänke and Dreibus (1988) and Agee et al. (2004); SiO_2 = 44.4, TiO_2 = 0.13, Al_2O_3 = 2.9, FeO = 17.9, MgO = 30.1, CaO = 2.4, Na_2O = 0.5, K_2O = 0.04, P_2O_5 = 0.17, Cr_2O_3 = 0.8). Starting materials for highly siderophile elements (Ru, Rh, Pd, Re, Os, Ir, Pt, Au) were powdered metals that were added to the mantle starting composition in equal abundances, at a total dopant level of 10 wt%. HSE have a very low solubility in silicate melts and even lower in silicate crystals if they exhibit incompatible behavior. Therefore, HSE were added at these higher wt% levels to make their concentrations higher and detectable in the silicate melts and the coexisting crystals. We know from our previous studies that addition of a few wt. % HSE makes the solubility levels high enough to be measured in the quenched silicate melts and crystals of the run products (e.g., Righter et al., 2004, 2015, 2018). At run conditions, HSE-Fe alloys formed separate droplets, but dissolved ppm levels of HSE in the silicate melt (see results section below). These concentrations (ppm) are higher than what is measured in natural samples (ppb), but still relevant to understanding and interpreting natural samples.

Experiments were carried out in the NASA JSC 880-ton multi-anvil press with a Walker module between 13 and 19 GPa, using the COMPRES 10/5 assembly (Leinenweber et al., 2012) in graphite capsules. The assembly was calibrated for pressure using SiO_2 transitions (at 9.4 GPa, 1600 °C), $(Mg_{82}Fe_{18})_2SiO_4$ transitions from olivine to wadsleyite (13.4 GPa, 1400 °C), and Mg_2SiO_4 transitions from wadsleyite to ringwoodite (15.0 GPa, 1200 °C, and 20.0 GPa, 1600 °C). The assembly utilizes injection molded octahedra, pyrophyllite gaskets, Re foil furnaces, and type C Re/W thermocouples (Righter et al., 2008b). Uncertainty in pressure and temperature are ±0.5

GPa and ±15-20 °C, respectively, based on temperature gradients no larger than 25 °C; thermocouple EMF has not been corrected for pressure effect. The runs were heated to between 1730 and 1770 ºC, held for 10-30 minutes, and quenched by cutting the power to the furnace (Table 1). The quenched samples were mounted in epoxy, cut and polished and examined by reflected light microscopy, Scanning Electron Microscopy (SEM), Electron Microprobe Analysis (EMPA), and Laser Ablation Inductively Coupled Plasma Mass Spectroscopy (LA-ICP-MS).

Analytical details

Backscattered electron (BSE) images were obtained using the JEOL LV-5910 and JF-7600 SEMs, and mineral compositional data were obtained using a Cameca SX-100 electron microprobe, all at NASA-JSC Crystals and quenched silicate melts from the run products were analyzed by EMPA for major and minor elements, using an accelerating voltage of 15 kV and sample current of 20 nA. Standards used included diopside (Ca), natural glass (Si, Al, Mg), rutile (Ti), rhodonite (Mn), chromite (Cr), apatite (P), albite (Na, Al), and potassium feldspar (K). Crystals were analyzed using a point beam, whereas multiphase quenched silicate melts were analyzed by rastering the beam over a 10 x 10 micron area for multiple different regions that were then averaged. Typical uncertainty for major elements analyzed by the NASA-JSC electron microprobe is < 2% (see also Righter et al., 2010).The concentrations of HSE, Sc, V, Cr, Mn, Co, Ni, Nb, Mo, and W in crystals and quenched silicate melts was determined by LA-ICP-MS at the Plasma Analytical Facility at Florida State University using an ESI New Wave™ UP193FX excimer laser ablation system coupled to a Thermo Element XR™ ICP-MS

(Yang et al., 2018). The samples were imaged with a reflected light microscope and scanning electron microscopy (SEM) at JSC, to avoid metal contamination in selected spots or tracks. 25 μm diameter spots and 15 μm wide lines were ablated at 50 Hz. Ablation times of 5 seconds were used for spots, while lines were scanned at 5 μm/s. Spots and lines were examined in time-resolved mode to check for metal contamination, and any datum indicating HSE spikes was removed prior to calculating average intensities. The abundances of the major elements, Sc, V, Cr, Co, Ni, Nb, Mo, W and HSEs were determined using a multi-standard approach discussed elsewhere (Humayun, 2012; Yang et al., 2015; Yang et al., 2018). Relative sensitivity factors were obtained using the Hoba (IVB) iron meteorite (Walker et al., 2008), the North Chile (Filomena, IIAB) iron meteorite (Wasson et al., 1989) and the NIST SRM 1263a steel for siderophile elements (Humayun et al., 2007; Gaboardi and Humayun, 2009; Humayun, 2012) and NIST SRM 610 glass, USGS basaltic glasses BHVO-2G, BIR-1G, and BCR-2G for lithophile elements (Jochum et al., 2011).

Results

Equilibrium

Several lines of evidence suggest that equilibrium was attained in these experiments. First, crystals and quenched liquids were homogeneous in major element composition as measured by EMPA, as opposed to showing zoning as might be expected in a system approaching equilibrium. Second, several elements yielded garnet/melt and olivine/melt partition coefficients that are consistent with previous work (see results

section below) at equivalent pressures and temperatures. And finally, in runs that contained garnet–melt and olivine–melt pairs, FeO–MgO partitioning was consistent with equilibrium attained in previous studies. For example, D(Fe) gt/melt = 0.42 to 0.74 compared to D(Fe) gt/melt = 0.37-0.99 and D(Mg) gt/melt = 0.45 to 0.98 compared to D(Mg) gt/melt = 0.83 to 2.17 from Yasuda et al., 1994; Herzberg and Zhang, 1996). Similarly, D(Fe) oliv/melt = 0.4 to 0.53 compared to D(Fe) oliv/melt = 0.48-0.50 and D(Mg) oliv/melt = 1.03 to 1.45 compared to D(Mg) oliv/melt = 1.47-1.49 from Herzberg and Zhang, 1996).

In addition to major elements, several refractory elements for which there are previous results for comparison, yield partitioning results that suggest an approach to equilibrium was achieved. For example, D(Sc) gt/melt is 2.2 to 3.4 in our experiments, overlapping with values measured in previous studies where equilibrium was also approached (Draper et al., 2003; Corgne et al., 2012; Suzuki and Akaogi, 1998). Similarly, our results for D(Pd), D(Pt) and D(Au) olivine/melt are all mildly to moderately incompatible, as also found by Righter et al. (2004) and Sharp et al. (2015) in which an approach to equilibrium was demonstrated. These comparable results suggest that even though we don't have diffusion data for HSE in these phases to establish equilibrium values using that approach, the levels measured in silicate phases, the homogeneity of the glasses, and the similar partition coefficients all point to an approach to equilibrium.

Oxygen fugacity of the experiments and relevance to the martian mantle

Using olivine-melt equilibria and Mg-Fe partitioning one can calculate the composition of olivine in equilibrium with melts in these experiments. Both experiments 207 and 258 contain olivine; using Kress and Carmichael (1991) to estimate liquid ferric/ferrous ratios at P, T, and variable oxygen fugacity (fO_2) combined with Snyder and Carmichael (1992) olivine-melt equilibrium show that the Fo_{92} and Fo_{95} olivines in these two experiments, respectively, are stable at IW+1. Such fO_2 agree with estimates for early martian mantle composition (Righter et al., 2008c; Shearer et al., 2006; Karner et al., 2007).

Phase equilibria

A summary of the experimental results is presented in Table 1. Experiments were done at 13, 14, 15, and 16 GPa. In the 13 GPa experiment (207), large 150 μm x 500 μm-sized garnets were stabilized at the center of the sample with adjacent large melt regions (**Figure 3A,B**). In the 14 GPa experiment (208) medium-sized (~200 μm) olivines were stable near the center of the sample container, adjacent to large melt regions on each side (**Figure 3C,D**). In one experiment at 15 GPa (258) olivine and garnet were stable, with olivine crystals 200 μm wide, but garnets typically 50-75 μm wide (**Figure 3E,F**). This experiment was nearer the solidus, as both olivine and garnet were stable, and less melt was present. In the other 15 GPa experiment (266), the overall sample was smaller and crystal-melt pairs were at the edges of the sample. Wadsleyite crystals stabilized in experiment 266 as ~ 30 x 100 μm in size (**Figure 3G,H**), and adjacent to melt patches. In the 16 GPa experiment (368), wadsleyite dominated the center of the capsule and was 100-200 μm in size, and in textural equilibrium with the melt portions above and below (**Figure 3I,J**).

All experiments contained metallic liquid droplets (e.g., **Figures 3A–J**), which represent HSE-Fe alloys that stabilized due to saturation of the silicate melts and crystals with the HSEs added as dopants. In studies of HSE partitioning in metal/silicate systems, HSE-rich nuggets are known to form and can compromise analyses of experimental results. Previous approaches have used repeated sampling of melts from a large crucible at low pressures, or analysis of multiple spots for comparison and potential identification of spikes or hot spots of HSE-rich material, or comparison of solubility of specific elements such as Pt, Pd, or Au (e.g., Borisov and Palme, 1994; Ertel et al., 2006) to those obtained independently where nuggets were known to be absent or minimized. Our new high pressure experiments are smaller in area and thus inherently less flexibility in evaluating the presence or influence of micro- or nano-nuggets. Interpretation of our results can only utilize the last approach which is comparison of measured concentrations to previous studies where nuggets were thought to be avoided or minimized. Our melts typically have 2.5 to 20 ppm Ru, 87 to 300 ppm Pd, and 10 to 300 ppm Au, all of which are comparable to levels measured in previous studies across this temperature range (e.g., Righter et al., 2015, 2018; Sharp et al., 2015). There is one exception - in experiment #258 an HSE nugget clearly interfered with the analysis of garnet resulting in concentrations as high as 30 to 335 ppm of some HSEs in the analysis. These are unreasonably high concentrations – higher than expected solubilities even in a silicate melt (e.g., Ertel et al., 2008), and thus are clearly due to a metallic HSE interference; this analysis was therefore excluded from the interpretation. All other HSE concentrations in melts from these experiments are within ranges expected for solubility in a silicate melt at these T and fO_2 conditions (e.g., Ertel et al., 2008; Righter et al., 2015). These

comparable values thus suggest that nugget effects have been minimized (but likely not completely eliminated) in these new experiments.

Partition coefficient values and comparison to previous results

Some key findings are highlighted here, but also the new results are tabulated along with previous studies for all trace elements in Supplementary Table S1. Element groupings are divided into lithophile, moderately siderophile and chalcophile, and the highly siderophile. Comparison to previous results are made where notable.

Lithophile – B, Sc, V, Cr, Mn, Sr, Y, Zr, Nb, Ba, La,

Boron is incompatible in wadsleyite, with D(B) = 0.06 and 0.3, not much different from D oliv/melt values near 0.1. D(Sc) gt/melt was found to be 2.2 and 3.4 in agreement with previous studies (**Figure 4A**), whereas D(Sc) oliv/melt = 0.02-1.23 and D(Sc) wads/melt = 0.46-0.87. Vanadium is incompatible in all phases, with D(V) from 0.05 to 0.42 (**Figure 4A**). Chromium is compatible in garnet with D=0.67 to 2.34 (**Figure 4A**), but incompatible in olivine and wadsleyite D=0.15 -0.32. Manganese is mildly incompatible in garnet with D=0.44-1.02 in contrast with Mn partitioning at 3 GPa where it is compatible in garnet, and more incompatible in olivine and wadsleyite with D = 0.23-0.41 compared with olivine at 1.5 - 3 GPa (Davis et al., 2013; LeRoux et al., 2011). Strontium is incompatible in garnet, olivine and wadsleyite with D = 0.047, 0.036, and 0.027, respectively. Finally, Y, Zr, Nb, Ba, and La are all highly incompatible in garnet (D<0.004 to 0.028), olivine (0.019 to 0.03 for Nb and 0.00042 and 0.00003,

respectively for Ba and La) and wadsleyite (0.019 for Y, 0.03 for Zr, 0.014 for Ba, and 0.029 for La), in agreement with previous studies (Supplementary Table S1).

Moderately siderophile and chalcophile – Ni, Co, Zn, Mo, W, Ga, Ge, and Cu

Cobalt is mildly incompatible to compatible with D(gt/melt) = 0.6, D(oliv/melt) = 0.87-0.94, and D(wads/melt) = 0.76-1.19. Nickel is similar to Cobalt with D(gt/melt) = 0.64 – 0.99, D(oliv/melt) = 0.42 to 1.51), and D(wads/melt) = 0.82-7.6. D(Ni) and D(Co) olivine/melt are both lower than measured in 1.5 to 2 GPa experiments of LeRoux et al. (2011), in which the values of 6-10, and 2-3, respectively. Zinc is incompatible in garnet (D=0.17) and olivine (D=0.36), and slightly more compatible in wadsleyite with D(Zn) = 0.39–0.56. In contrast, at pressures <3 GPa, Zn has D~1 in olivine and is compatible in spinel (Davis et al., 2013). D(Mo) and D(W) gt/melt were 0.07, slightly higher than measured by Righter and Shearer (2003), while D(W) oliv/melt = 0.0017 in good agreement with Righter and Shearer (2003). Gallium is compatible in garnet with D=2.8 in agreement with previous work (Righter and Drake, 2000; **Figure 4A**), incompatible in olivine, and mildly incompatible to compatible in wadsleyite D=0.11 to 1.38. At 3 GPa, Davis et al. (2013) found Ga to be incompatible in garnet but strongly compatible in spinel. We surmise that the higher D(Ga) and D(Zn) observed in wadsleyite relative to olivine may be related to its spinelloid structure. Germanium is mildly incompatible in wadsleyite D = 0.46 (similar to its low pressure partitioning in olivine (Davis et al., 2013; Yang et al., 2015; Righter et al., 2018). Finally, Copper is incompatible in garnet and olivine, with slightly more compatibility in wadsleyite with D(Cu) = 0.11–1.02, comparable to D(Cu) majorite/melt = 0.6 from Yurimoto and Ohtani (1992).

Highly siderophile – Ru, Rh, Pd, Re, Os, Ir, Pt, Au

D(Ru) garnet/melt and olivine/melt are incompatible with values of 0.14 for garnet and 0.03 and 0.13 for oliv/melt. Ruthenium is slightly higher for wads/melt with D = 0.58. Notably, D(Ru) oliv/melt is lower at high pressures; usually near 1 at low P, but ~0.1 at high P (Brenan et al. 2003; Righter et al. 2004; Sharp et al. 2015; **Figure 4B**). Sharp et al. (2015) discussed the possibility that pressure may lower the value of D(Ru) olivine/melt (at constant fO_2), or that a change in Ru valence state occurs over this range of fO_2 that could account for the stabilization of the partition coefficient below log fO_2 = -5. Our results suggest that pressure may be an important variable, since our highest pressure olivine-melt experiments are at 14 GPa, where D(Ru) = 0.03 to 0.13 (Table 2), but similar oxygen fugacity to the Sharp et al. (2015) experiment. On the other hand, D(Ru) is much higher for wadsleyite/melt with values near 0.6 (**Figure 4B**). The greater compatibility in spinel-structured wadsleyite is perhaps not unexpected given the compatibility of Ru in magnesioferrite and chromite (Righter and Downs, 2001; Righter et al., 2004).

Rhodium and Pd exhibit similar partitioning behavior to Ru and both are incompatible in garnet and olivine, with values all < 0.25. Both D(Rh) and D(Pd) wads/melt are slightly higher with values of 0.29 and 0.41, respectively. Rhenium is largely incompatible in all phases, with garnet/melt = 0.31 being the highest value. These relatively low values compare with the mildly incompatible values for Re partitioning in many common magmatic minerals (e.g., Righter et al., 2004; Mallmann and O'Neill, 2007). Osmium is more compatible than Re in every phase, with values from 0.76 in garnet, 2.4 in olivine, and 0.33 in wadsleyite. D(Ir) values are similar to those for Os. D(Pt) garnet/melt = 1.78, but lower and all near 0.1 for other phases. Finally, D(Au) is

low between 0.01 (oliv) to 0.13 for all other phases. Although one might argue that the high D(oliv/melt) for Os, Ir, and Ru might be due to micronugget inclusions, all three of these elements are known to be compatible to mildly incompatible in basic systems. For example, analysis of Puchtel et al. (2001) on separated olivine from a komatiitic basalt lava lake revealed that Ru, Os, and Ir were slightly compatible to moderately incompatible in olivine (D= 1.7–0.8), in general agreement but also indicating a slight increase in compatibility with pressure for Os.

Discussion

Potential for HSE, Sc, and V fractionation in magma ocean setting

Magma oceans are thought to have been common on early solar system bodies, for thermal (Tonks and Melosh, 1993) and chemical (Righter, 2003; Righter and Drake, 1996) reasons, and are part of the current paradigm for differentiated bodies (Elkins-Tanton, 2012; Greenwood, et al., 2005). As a magma ocean cools and crystallizes, there is potential for fractionation of HSE as mantle phases crystallize out of the molten mantle. HSE are highly compatible in metal and sulfide and thus if either of these phases crystallizes out of a magma ocean, the HSE concentrations will be substantially effected. Metal segregation from a magma ocean is efficient and metal is not likely to saturate and fractionate in the magma ocean stage once a core has formed (Rushmer et al., 2000). Sulfide fractionation has been proposed for the early Earth (O'Neill, 1991) and can occur in the deepest part of the terrestrial magma ocean if S levels reach those of sulfide saturation (SCSS) (e.g., Righter et al., 2018). Therefore, it is not unreasonable to

consider sulfide fractionation from a martian magma ocean. However, sulfide saturation represents a challenge for several reasons. First, the FeO-rich martian mantle (18 wt% FeO) means that it will have a very high SCSS, estimated to be 2200 ppm at 15 GPa ranging up to 4300 ppm at 2 GPa based on the appropriately high FeO melt compositions of Li and Agee (1996, 2001). These values are higher than estimates of the S content of the post-core formation mantle. For example, using the core mass fraction of 0.21 (Longhi et al., 1992), bulk S content of 2.2 % (Lodders and Fegley, 1997), and a D(S) metal/silicate partition coefficient of 94 (calculated using the predictive expression of Boujibar et al. (2014) for a Wänke and Dreibus (1988) primitive mantle composition, 15 GPa, 2400 °C, and IW-1.5), results in S content of 975 ppm. Even if the bulk composition was increased to 3 wt% S, the corresponding S content of the magma ocean would be 1400 ppm. These values are in the same range as estimates of 390 ppm (Sanloup et al., 1999), 900 ppm (Lodders and Fegley, 1997), <700-1000 ppm (Ding et al., 2015), and 1050 ppm (Yang et al., 2020). Even with a substantial amount of crystallization and the S content of the magma ocean increasing, the depth (and pressure) of the magma ocean will decrease which causes the SCSS to increase to even higher values. For these reasons, sulfide saturation and fractionation in a martian magma ocean is unrealistic.

Because metal and sulfide are not reasonable fractionating phases in a martian magma ocean, the role of silicates becomes central to understanding possible fractionation of HSEs. Because silicate liquids are compressible compared to mantle minerals such as olivine and garnet, there can be density crossovers in deep magma oceans that lead to fractionation of a phase such as olivine or garnet (Agee, 2008). As a

magma ocean cools and crystallizes, there is potential for further fractionation of mantle phases as they crystallize out of the molten mantle. The new results here enable examination of these two portions of the early history of Mars – we look at the potential for garnet or olivine fractionation on specific HSE ratios, and then model the crystallization of a martian magma ocean, looking at the concentrations of HSE in the cumulate solids and liquids as crystallization proceeds. Examining Re/Os and Pt/Os ratios, combined with other lithophile isotopic systems such as Lu/Hf, Sm/Nd, and Rb/Sr, will allow evaluation of how super– and sub-chondritic early martian Os isotopic reservoirs were generated.

Sc and V are both refractory elements not affected by volatilization processes. Because mineral/melt V partitioning is sensitive to fO_2 variation, and Sc is not, V/Sc ratios in mantle melts have been used to calculate the fO_2 of terrestrial mantle sources (Li and Lee, 2004; Mallmann and O'Neill, 2009). Application to martian mantle is hindered due to a lack of direct samples of the martian mantle. However, there is general agreement that the martian mantle experienced a deep magma ocean that could have fractionated Sc and V. Our new results can be used to place some limits on the extent of fractionation.

Estimates of bulk silicate Mars (BSM) include Sc = 11 ppm and V = 60 ppm, yielding a V/Sc ratio of 5.5. Our results show that Sc is compatible in majoritic garnet, and wadsleyite, whereas V is compatible in garnet but incompatible in wadsleyite. This results in deep mantle melting partition coefficients of D(Sc) = 1.25; D(V) = 0.24 (25% majoritic garnet, 5% clinopyroxene, and 60% wadsleyite; see modelling section below). Deep mantle fractionation will thus make a magma ocean richer in V and poorer in Sc,

and thus increase V/Sc compared to bulk silicate Mars. This would change V/Sc from 5.5 to 8.1 if the mantle were 65% molten with the solid mantle comprised of 25% majoritic garnet, 5% clinopyroxene, and 60% wadsleyite. This range of V/Sc corresponds to approximately 1 log fO_2 unit for the V/Sc barometer of Li and Lee (2004), so there is some uncertainty in application to the martian mantle. However, ***relative*** differences in V/Sc between martian basalts could nonetheless be useful, and it is interesting to note that the most reduced and depleted shergottites – QUE 94201 and NWA 5990 – both have very low V/Sc ratios (2.5-2.8; Warren et al., 1999; Yang et al., 2015) that would be expected of reduced mantle melts (~FMQ-3). Furthermore, the most oxidized and enriched shergottites – LAR 06319 and NWA 1068 – also have higher V/Sc ratios of 6.7 to 7.6 (Barrat et al., 2002; Sarbadhikari et al., 2009) as would be expected in oxidized melts (~FMQ-1). It seems that this barometer could be calibrated for application specifically to Mars and has not been compromised by deep mantle fractionation.

Fractionation of HSEs in a floatation layer

Because of the FeO-rich nature of martian mantle and thus melts derived therefrom, martian mantle melts will be relatively dense and crystallizing silicates will be buoyant at shallower depths than for Earth, for example (Stolper et al., 1981). This has allowed the possibility of olivine or garnet floatation layers in the crystallizing martian magma ocean, which could in some scenarios lead to major and trace element fractionation of the residual melts. Ratios of incompatible HSE (IHSE - Re, Pd, Au) vs. compatible HSE (CHSE - Ir, Os) may be sensitive to fractionation of garnet or olivine from a molten mantle. We will use our results to evaluate the extent of elemental

fractionation of HSE (IHSE/CHSE ratios) if garnet or olivine is segregated from the magma ocean.

Garnet is well known to cause fractionation of some lithophile elements such as Sc and light REE (Sm) or heavy REE (Yb). This is due to the regular behavior of REE in garnet/melt partitioning (van Westrenen and Draper, 2007). Walter et al. (2004) demonstrated the effect of garnet fractionation on the primitive terrestrial mantle ratios of some of these elements. Re/Os and Pd/Ir are common indicators of fractionation amongst the HSE (Righter et al., 2000). It is clear from our results that all four of these elements have similar degrees of incompatibility, so that the ratios are not fractionated substantially by olivine or garnet crystallization. Pd/Ir and Re/Os both exhibit very small changes with garnet or olivine fractionation, indicating that fractionation of either of these phases will not change the ratios significantly (**Figure 5a,b**). Because Pt is mildly compatible in garnet, the Pt/Os ratio can be fractionated by ~5% after 20% garnet fractionation from a magma ocean, but this is also relatively small because Os is also compatible in garnet. Olivine fractionation, on the other hand, will not cause significant fractionation in Pt/Os in an olivine flotation layer (**Figure 5c**).

The survival of such elemental fractionations is a different question. During equilibrium crystallization, and rigorous convection, there may be limited exchange between such a floatation layer and the melts above and below (Reese and Solomotov, 2006). However, when the mantle becomes fully crystalline, other processes may ensue such as solid state convection (Jacobsen and Yu, 2015) and even mantle overturn due to density differences (Scheinberg et al., 2014). We will not evaluate these processes, but

simply show that there is limited IHSE/CHSE fractionation with olivine segregation, and only slightly more potential with garnet segregation.

Evolution of Re/Os in martian magma ocean and generation of mantle reservoirs

A deep martian magma ocean was proposed as a possibility by Righter and Drake (1996), and subsequently re-evaluated by Righter et al. (1998), Righter and Drake (2000), Righter and Chabot (2011), Rai and vanWestrenen (2013), Yang et al. (2015), and Righter et al. (2015). These studies have narrowed the pressure-temperature range of the base of the magma ocean to 14+/-3 GPa, and 2300 +/- 200 K. Independently, Lu-Hf and Sm-Nd isotopic data for martian meteorites suggests that an enriched martian mantle can be produced by mixing of trapped magma ocean melt and depleted cumulates (Debaille et al., 2008). The best fit to the elemental and isotopic data is for deep mantle mineralogy – with a pressure near 15 GPa. So, there is evidence from both lithophile and siderophile elements for a major mantle differentiation event at this PT range or depth in the early martian mantle. This is an interesting PT range because it is close to the transformation of a shallow garnet-pyroxene-olivine mantle to that of a majorite-wadsleyite dominated mantle near 13-14 GPa (Bertka and Fei, 1998; Khan and Connolly, 2008, Khan et al., 2018). Thus our partitioning results can be used to calculate the Re/Os and Pt/Os (and other HSE ratios) of an evolving liquid during crystallization of a deep magma ocean. The results can then be used to evaluate if such a deep magma ocean cumulates and residual liquids are consistent with the Re-Os systematics of martian shergottites and postulated sources.

The Re, Pt, and Os concentrations of the post core-formation magma ocean can be calculated using metal-silicate equilibrium partitioning (Righter et al., 2015). Although the post core-formation mantle is similar in Re, Pt, and Os content to estimates of primitive martian mantle (PMM), and Righter et al. (2015) argue the PMM may hold a record of core formation (rather than a late veneer or late accretion), the uncertainty in the values calculated from experimental data is high. Even though Tait and Day (2018) argue that the high pressure calculated mantle has an unreasonable sub-chondritic Re/Os ratio, the uncertainty in these calculated Re and Os contents is higher than those from isotopic constraints. Furthermore, the crystallization of the magma ocean is likely to create sub- and super-chondritic reservoirs. Deviations from that mantle must be present, to explain all isotope data, and thus crystallization and melting of martian mantle should be evaluated as a mechanism for Re/Os and Pt/Os fractionation.

The magma ocean will undergo equilibrium crystallization including entrainment of crystals in convective flow throughout much of the crystallization sequence, until convective lock-up is attained at a small % of residual liquid. Thus, we can use the phase relations of the modeled martian mantle composition at low P (30%gt-10%cpx-60%oliv) and high P (35%maj-5%cpx-60%wads) from Khan et al. (2018), in combination with HSE partitioning data from our study and tabulated and compiled by Righter et al. (2015) and Sharp et al. (2015), to calculate the HSE content of the evolving liquid. Using a simple modal crystallization model, bulk D that is an average of the low and high pressure mantle minerals (from this work and Table 3), and the HSE content of the magma ocean as initial mantle concentrations (from Righter et al., 2015), the HSE concentrations of liquids and solids can be calculated as crystallization proceeds. The

Os, Pt, and Ir contents of the liquids stay nearly constant due to the mildly incompatible or slightly compatible behavior of these three elements. On the other hand, Re, Ru, and especially Au and Pd all increase substantially during crystallization by factors of 5-20 (**Figure 6**). These increases relative to the compatible HSE, will thus produce liquids with super-chondritic Re/Os, and higher Pd/Ir than the original magma ocean (or mantle). Such super-chondritic Re/Os liquids in the mantle will thus be available for incorporation into a shergottite reservoir and acquire positive γOs. Similarly, the solids would have sub-chondritic Re/Os and very low Pd/Ir and thus be capable of producing or contributing to reservoirs that acquire negative γOs. These results are similar to those of Brandon et al. (2012), except that those authors used mantle melting partition coefficients of D(Re) and D(Os) of 1.2 and 7.9, respectively (Table 3). Although our results support the less compatible nature of Re compared to Os, ours clearly show that Re is incompatible and Os is mildly compatible. The values used by Brandon et al. (2012) were arbitrarily chosen to re-produce the shergottite data, but they are not consistent with available and new (this study) partitioning data for these elements.

In summary, our new results predict the formation of super and sub-chondritic Re/Os portion of the martian mantle as a deep magma ocean crystallized; the crystallizing magma ocean is a process that can help to generate the positive and negative γOs anomalies in the early martian mantle (Brandon et al., 2012; Tait and Day, 2018). The success of such models depends on the ability to explain lithophile isotopic data and this will be evaluated below.

Linking Os with Nd, Lu and Sr isotopes

Os isotopic values for shergottite source regions correlate with other long-lived and lithophile isotopic systems such as Sm/Nd, Lu/Hf and Rb/Sr (**Figure 2**). Correlations between Nd-Hf-Sr isotopes can be explained by melting of mantle comprised of a mixture of residual liquids and solids from the martian magma ocean (DeBaille et al., 2008; Lapen et al., 2017). Using the calculations from the previous section, our new results can be used to evaluate whether Re-Os isotopes are consistent with such a scenario. We utilize partitioning data for Sm/Nd, Lu/Hf and Rb/Sr (Table 3), together with our crystallization modelling, to calculate Sm/Nd, Lu/Hf and Rb/Sr in the liquids and solids (**Figure 7**). Sm/Nd and Lu/Hf of the solids start high (during crystallization) and end lower; the liquids have subchondritic Sm/Nd and Lu/Hf, whereas the solids have superchondritic Sm/Nd and Lu/Hf (Fig 7). In contrast, Rb/Sr and Re/Os exhibit the opposite behavior due to the parent isotope having incompatible behavior relative to the daughter. Therefore, liquids evolve to generally super-chondritic Rb/Sr and Re/Os and solids have subchondritic Rb/Sr and Re/Os. This contrasting behavior leads to specific expected correlations in these isotopic systems. As an example, we examine Nd-Os using our model results. Residual solids from a magma ocean will have high Sm/Nd and low Re/Os, whereas the liquids will have low Sm/Nd and relatively high Re/Os (**Figure 8**). Mixtures of these two end members can easily explain the range of Re/Os and Sm/Nd measured in shergottite suites. Comparison of Sm-Nd and Re-Os shows that mixtures of liquids and solids remaining after 95-99% crystallization fall outside the field of enriched and depleted shergottites (**Figure 8**). However, mixtures of 25-45% solid with residuals liquids would be able to reproduce the range of values seen

in the shergottite suite. These results are similar to the conclusions of Debaille et al. (2008) and would explain the range of Os isotopic values reported for shergottites by Brandon et al. (2012).

Future work

Particular emphasis on magnesiowüstite is deserved as it is already known that some HSE have a preference for oxide structures (e.g., Righter and Downs, 2001; Righter et al., 2004a; Brenan et al., 2012). There has been some work on the relative compatibility of Re and Os in magnesiowüstite (Fortenfant et al., 2003), but silicate melt was notably absent from those experiments which consisted of magnesiowüstite-metal pairs. However, there is a clear preference for Re over Os in magnesiowüstite, which is opposite the behavior of many low pressure phases such as olivine and spinel (e.g., Righter et al., 2004; Mallmann and O'Neill, 2007). Future efforts might also focus on ringwoodite and akimotoite partitioning to see if any phases can fractionate HSEs to the extent observed in post core-formation mantle, and to evaluate effects of cumulate overturn that might involve these phases.

Acknowledgements

This work was supported by NASA Planetary Science Division and an RTOP (KR) from the NASA Cosmochemistry program. The manuscript benefitted from reviews of two anonymous reviewers and the AE A. Yamaguchi.

References:

Agee, C.B. (2008) Compressibility of water in magma and the prediction of density crossovers in mantle differentiation. *Philosophical Transactions of the Royal Society A: Mathematical, Physical and Engineering Sciences 366*, 4239-4252.

Agee, C.B. and Draper, D.S. (2004) Experimental constraints on the origin of Martian meteorites and the composition of the Martian mantle. *Earth and Planetary Science Letters 224*, 415-429.

Barnes, J.J., McCubbin, F.M., Santos, A.R., Day, J.M., Boyce, J.W., Schwenzer, S.P., Ott, U., Franchi, I.A., Messenger, S., Anand, M. and Agee, C.B. (2020) Multiple early-formed water reservoirs in the interior of Mars. *Nature Geoscience* 13, 260–264.

Barrat, J.A., Jambon, A., Bohn, M., Gillet, P., Sautter, V., Göpel, C., Lesourd, M. and Keller, F. (2002) Petrology and chemistry of the picritic shergottite North West Africa 1068 (NWA 1068). *Geochimica et Cosmochimica Acta 66*, 3505-3518.

Bertka, C. M., & Fei, Y. (1998) Density profile of an SNC model Martian interior and the moment-of-inertia factor of Mars. *Earth and Planetary Science Letters 157*, 79-88.

Borisov, A., Palme, H., & Spettel, B. (1994) Solubility of palladium in silicate melts: implications for core formation in the Earth. *Geochimica et Cosmochimica Acta* 58, 705-716.

Boujibar, A., Andrault, D., Bouhifd, M. A., Bolfan-Casanova, N., Devidal, J. L., and Trcera, N. (2014) Metal–silicate partitioning of sulphur, new experimental and thermodynamic constraints on planetary accretion. *Earth and Planetary Science Letters 391*, 42-54.

Brandon, A.D., Puchtel, I.S., Walker, R.J., Day, J.M., Irving, A.J., and Taylor, L.A. (2012) Evolution of the martian mantle inferred from the ^{187}Re–^{187}Os isotope and highly siderophile element abundance systematics of shergottite meteorites. *Geochimica et Cosmochimica Acta 76*, 206-235.

Brandon, A.D., Walker, R.J., Morgan, J.W., and Goles, G.G. (2000) Re-Os isotopic evidence for early differentiation of the Martian mantle. *Geochimica et Cosmochimica Acta* 64, 4083-4095.

Brasser, R. and Mojzsis, S.J. (2017) A colossal impact enriched Mars' mantle with noble metals. *Geophysical Research Letters 44*, 5978-5985.

Brenan, J.M., McDonough, W.F., and Dalpe, C. (2003) Experimental constraints on the partitioning of rhenium and some platinum group elements between olivine and silicate melt. *Earth Planet. Sci. Lett.* 212, 135-150.

Brenan, J.M., McDonough, W.F., and Ash, R. (2005) An experimental study of the solubility and partitioning of iridium, osmium and gold between olivine and silicate melt. *Earth and Planetary Science Letters* 237, 855-872.

Brenan, J.M., Finnigan, C.F., McDonough, W.F., and Homolova, V. (2012) Experimental constraints on the partitioning of Ru, Rh, Ir, Pt and Pd between chromite and silicate melt: the importance of ferric iron. *Chemical Geology 302*, 16-32.

Brennan, M. C., Fischer, R. A., and Irving, J. C. (2020) Core formation and geophysical properties of Mars. *Earth and Planetary Science Letters* 530, 115923.

Corgne, A., Armstrong, L. S., Keshav, S., Fei, Y., McDonough, W. F., Minarik, W. G., & Moreno, K. (2012) Trace element partitioning between majoritic garnet and silicate melt at 10–17 GPa: Implications for deep mantle processes. *Lithos 148*, 128-141.

Davis, F. A., Humayun, M., Hirschmann, M. M., & Cooper, R. S. (2013) Experimentally determined mineral/melt partitioning of first-row transition elements (FRTE) during melting of peridotite at 3 GPa. *Geochimica et Cosmochimica Acta 104*, 232-260.

Day, J. M., Brandon, A. D., & Walker, R. J. (2016) Highly siderophile elements in Earth, Mars, the Moon, and asteroids. *Reviews in Mineralogy and Geochemistry 81*, 161-238.

Debaille, V., Brandon, A.D., Yin, Q.Z., and Jacobsen, B. (2007) Coupled ^{142}Nd-^{143}Nd evidence for a protracted magma ocean in Mars. *Nature* 450, 525-528.

Debaille, V., Brandon, A.D., Yin, Q.Z., and Jacobsen, B. (2008) Martian mantle mineralogy investigated by the ^{176}Lu-^{176}Hf and ^{147}Sm-^{143}Nd systematics of shergottites. *Earth Planet. Sci. Lett.* 269, 186-199.

Ding, S., Dasgupta, R., Lee, C.T.A., and Wadhwa, M. (2015) New bulk sulfur measurements of Martian meteorites and modeling the fate of sulfur during melting and crystallization–Implications for sulfur transfer from Martian mantle to crust–atmosphere system. *Earth and Planetary Science Letters 409*, 157-167.

Draper, D.S., Xirouchakis, D., and Agee, C.B. (2003) Trace element partitioning between garnet and chondritic melt from 5 to 9 GPa: implications for the onset of the majorite

transition in the martian mantle. *Physics of the Earth and Planetary Interiors 139*, 149-169.

Elkins-Tanton, L.T. (2012) Magma oceans in the inner solar system. *Annual Review of Earth and Planetary Sciences 40*, 113-139.

Elkins-Tanton, L. T., E. M. Parmentier, and P. C. Hess (2003) Magma ocean fractional crystallization and cumulate overturn in terrestrial planets: Implications for Mars. *Meteoritics & Planetary Science* 38, 1753-1771.

Elkins-Tanton, L.T., Hess, P.C., and Parmentier, E.M. (2005a) Possible formation of ancient crust on Mars through a magma ocean processes. *Jour. Geophys. Res.* 110, E12S01.

Elkins-Tanton, L.T., Zaranek, S.E., Parmentier, E.M. and Hess, P.C. (2005b) Early magnetic field and magmatic activity on Mars from magma ocean cumulate overturn. *Earth Planet. Sci. Lett.* 236, 1-12.

Ertel, W., Walter, M.J., Drake, M.J., and Sylvester, P.J. (2006) Experimental study of platinum solubility in silicate melt to 14 GPa and 2273 K: Implications for accretion and core formation in Earth. *Geochimica et Cosmochimica Acta* 70, 2591-2602.

Ertel, W., Dingwell, D. B., & Sylvester, P. J. (2008) Siderophile elements in silicate melts—A review of the mechanically assisted equilibration technique and the nanonugget issue. *Chemical Geology 248*, 119-139.

Fortenfant, S.S., Rubie, D.C., Reid, J., Dalpe, C., Capmas, F., and Gessmann, C.K. (2003) partitioning of Re and Os between liquid metal and magnesiowüstite at high pressure. *Phys. Earth Planet. Int.* 139, 77-91.

Gaboardi, M. and Humayun, M. (2009) Elemental fractionation during LA-ICP-MS analysis of silicate glasses: Implications for matrix-independent standardization. *Journal of Analytical Atomic Spectrometry* 24, 1188-1197.

Greenwood, R.C., Franchi, I.A., Jambon, A., and Buchanan, P.C. (2005) Widespread magma oceans on asteroidal bodies in the early solar system. *Nature 435*, 916-20.

Humayun, M., Simon, S. B., and Grossman, L. (2007) Tungsten and hafnium distribution in calcium–aluminum inclusions (CAIs) from Allende and Efremovka. *Geochimica et Cosmochimica Acta* 71, 4609-4627.

Humayun, M. (2012) Chondrule cooling rates inferred from diffusive profiles in metal lumps from the Acfer 097 CR2 chondrite. *Meteoritics & Planetary Science* 47, 1191-1208.

Jacobsen, S.B. and Yu, G. (2015) Extinct isotope heterogeneities in the mantles of Earth and Mars: Implications for mantle stirring rates. *Meteoritics & Planetary Science 50*, 555-567.

Jochum, K. P., Weis, U., Stoll, B., Kuzmin, D., Yang, Q., Raczek, I., ... and Günther, D. (2011) Determination of reference values for NIST SRM 610–617 glasses following ISO guidelines. *Geostandards and Geoanalytical Research* 35, 397-429.

Karner, J. M., Papike, J. J., Shearer, C. K., McKay, G., Le, L., & Burger, P. (2007) Valence state partitioning of Cr and V between pyroxene-melt: Estimates of oxygen fugacity for martian basalt QUE 94201. *American Mineralogist 92*, 1238-1241.

Khan, A. and Connolly, J.A.D. (2008) Constraining the composition and thermal state of Mars from inversion of geophysical data, *J. Geophys. Res.*, 113, E07003, doi:10.1029/2007JE002996.

Khan, A., Liebske, C., Rozel, A., Rivoldini, A., Nimmo, F., Connolly, J. A. D., ... & Giardini, D. (2018) A geophysical perspective on the bulk composition of Mars. *Journal of Geophysical Research: Planets 123*, 575-611.

Kleine, T., Mezger, K., Münker, C., Palme, H., and Bischoff, A. (2004) ^{182}Hf-^{182}W isotope systematics of chondrites, eucrites, and martian meteorites: Chronology of core formation and early mantle differentiation in Vesta and Mars. *Geochim. Cosmochim Acta* 68, 2935-2946.

Kress, V. C., & Carmichael, I. S. (1991) The compressibility of silicate liquids containing Fe_2O_3 and the effect of composition, temperature, oxygen fugacity and pressure on their redox states. *Contributions to Mineralogy and Petrology 108*, 82-92.

Lapen, T.J., Righter, M., Andreasen, R., Irving, A.J., Satkoski, A.M., Beard, B.L., Nishiizumi, K., Jull, A.T. and Caffee, M.W. (2017) Two billion years of magmatism recorded from a single Mars meteorite ejection site. *Science advances*, *3*(2), p.e1600922.

Leinenweber, K.D., Tyburczy, J.A., Sharp, T.G., Soignard, E., Diedrich, T., Petuskey, W.B., ... and Mosenfelder, J.L. (2012) Cell assemblies for reproducible multi-anvil experiments (the COMPRES assemblies). *American Mineralogist 97*, 353-368.

Le Roux, V., Dasgupta, R., and Lee, C.T. (2011) Mineralogical heterogeneities in the Earth's mantle: constraints from Mn, Co, Ni and Zn partitioning during partial melting. *Earth and Planetary Science Letters 307*, 395-408.

Li, Z.X.A. and Lee, C.T.A. (2004) The constancy of upper mantle fO_2 through time inferred from V/Sc ratios in basalts. *Earth and Planetary Science Letters* 228, 483-493.

Li, J. and Agee, C.B. (1996) Geochemistry of mantle–core differentiation at high pressure. *Nature 381*, 686-689.

Li, J. and Agee, C.B. (2001) Element partitioning constraints on the light element composition of the Earth's core. *Geophysical Research Letters 28*, 81-84.

Lodders, K., & Fegley Jr, B. (1997) An oxygen isotope model for the composition of Mars. *Icarus 126*, 373-394.

Longhi, J., Knittle, E., Holloway, J. R., and Wänke, H. (1992) The bulk composition, mineralogy, and internal structure of Mars. In H.H. Kieffer, B.M. Jakosky, C.W. Snyder, and M.S. Matthews (Eds), *Mars*, University of Arizona Press, Tucson, AZ, 184-208.

Mallmann, G. and O'Neill, H.St.C. (2007) The effect of oxygen fugacity on the partitioning of Re between crystals and silicate melt during mantle melting. *Geochim. Cosmochim. Acta* 71, 2837-2857.

Mallmann, G. and O'Neill, H.S.C. (2009) The crystal/melt partitioning of V during mantle melting as a function of oxygen fugacity compared with some other elements (Al, P, Ca, Sc, Ti, Cr, Fe, Ga, Y, Zr and Nb). *Journal of Petrology* 50, 1765-1794.

Malavergne, V., Charon, E., Jones, J., Cordier, P., Righter, K., Deldicque, D., & Hennet, L. (2016) The formation of nuggets of highly siderophile elements in quenched silicate melts at high temperatures: Before or during the silicate quench?. *Earth and Planetary Science Letters 434*, 197-207.

Marchi, S., Walker, R. J., & Canup, R. M. (2020) A compositionally heterogeneous martian mantle due to late accretion. *Science advances*, *6*(7), eaay2338.

Mibe, K., Orihashi, Y., Nakai, S. I., & Fujii, T. (2006) Element partitioning between transition-zone minerals and ultramafic melt under hydrous conditions. *Geophysical Research Letters 33*.

Moriwaki, R., Usui, T., Tobita, M., and Yokoyama, T. (2020) Geochemically heterogeneous Martian mantle inferred from Pb isotope systematics of depleted shergottites. *Geochimica et Cosmochimica Acta 274*, 157-171.

O'Neill, H. S. C. (1991) The origin of the Moon and the early history of the Earth—A chemical model. Part 2: The Earth. *Geochimica et Cosmochimica Acta 55*, 1159-1172.

Parmentier, E.M. and Zuber, M.T. (2007) Early evolution of Mars with mantle compositional stratification or hydrothermal crustal cooling. *Journal of Geophysical Research: Planets*, *112*(E2).

Puchtel, I.S. and Humayun, M. (2001) Platinum group element fractionation in a komatiitic basalt lava lake. *Geochimica et Cosmochimica Acta 65*, 2979-2993.

Rai, N. and van Westrenen, W. (2013) Core-mantle differentiation in Mars. *Journal of Geophysical Research: Planets 118*, 1195-1203.

Reese, C.C. and Solomotov, V.S. (2006) Fluid dynamics of local martian magma oceans. *Icarus* 184, 102-120.

Righter, K. (2003) Metal-silicate partitioning of siderophile elements and core formation in the early Earth. *Annual Review of Earth and Planetary Sciences 31*, 135-174.

Righter, K., & Chabot, N. L. (2011) Moderately and slightly siderophile element constraints on the depth and extent of melting in early Mars. *Meteoritics & Planetary Science 46*, 157-176.

Righter, K., and R.T. Downs (2001) The crystal structures of synthetic Re- and PGE-bearing magnesioferrite spinels: Implications for impacts, accretion and the mantle, *Geophys. Res. Lett.* 28, 619–622.

Righter, K. and Drake, M.J. (1996) Core formation in Earth's moon, Mars, and Vesta. *Icarus 124*, 513-529.

Righter, K. and Drake, M. J. (2000) Metal/silicate equilibrium in the early Earth—New constraints from the volatile moderately siderophile elements Ga, Cu, P, and Sn. *Geochimica et Cosmochimica Acta 64*, 3581-3597.

Righter, K. and Shearer, C. K. (2003) Magmatic fractionation of Hf and W: constraints on the timing of core formation and differentiation in the Moon and Mars. *Geochimica et Cosmochimica Acta 67*, 2497-2507.

Righter, K., Hervig, R., and Kring, D. (1998) Accretion and core formation on Mars: Molybdenum contents of melt inclusion glasses in three SNC meteorites. *Geochimica et Cosmochimica Acta 62*, 2167-2177.

Righter, K., Walker, R. J., and Warren, P. H. (2000) Significance of highly siderophile elements and osmium isotopes in the lunar and terrestrial mantles. *Origin of the Earth and Moon*, 291-322.

Righter, K., Campbell, A.J., Humayun, M., and R.L. Hervig (2004) Partitioning of Re, Ir, Rh, and Ru between Cr-bearing spinel, olivine, pyroxene and silicate melts. *Geochim. Cosmochim. Acta* 68, 867-880.

Righter, K., Chesley, J. T., Caiazza, C. M., Gibson Jr, E. K., and Ruiz, J. (2008a) Re and Os concentrations in arc basalts: the roles of volatility and source region fO_2 variations. *Geochimica et Cosmochimica Acta 72*, 926-947.

Righter, K., Humayun, M., and Danielson, L. (2008b) Partitioning of palladium at high pressures and temperatures during core formation. *Nature Geoscience*, *1*(5), 321-323.

Righter, K., Yang, H., Costin, G., and Downs, R.T. (2008c) Oxygen fugacity in the Martian mantle controlled by carbon: New constraints from the nakhlite MIL 03346. *Meteoritics & Planetary Science 43*, 1709-1723.

Righter, K., Pando, K., & Danielson, L.R. (2009) Experimental evidence for sulfur-rich martian magmas: Implications for volcanism and surficial sulfur sources. *Earth and Planetary Science Letters 288*, 235-243.

Righter, K., Pando, K. M., Danielson, L., & Lee, C. T. (2010) Partitioning of Mo, P and other siderophile elements (Cu, Ga, Sn, Ni, Co, Cr, Mn, V, and W) between metal and silicate melt as a function of temperature and silicate melt composition. *Earth and Planetary Science Letters 291*, 1-9.

Righter, K., Danielson, L.R., Pando, K.M., Williams, J., Humayun, M., Hervig, R. L., and Sharp, T. G. (2015) Highly siderophile element (HSE) abundances in the mantle of Mars are due to core formation at high pressure and temperature. *Meteoritics & Planetary Science 50*, 604-631.

Righter, K., Pando, K., Marin, N., Ross, D.K., Righter, M., Danielson, L., Lapen, T.J. and Lee, C. (2018) Volatile element signatures in the mantles of Earth, Moon, and Mars: Core formation fingerprints from Bi, Cd, In, and Sn. *Meteoritics & Planetary Science 53*, 284-305.

Righter, K., Pando, K., Ross, D. K., Righter, M., & Lapen, T. J. (2019) Effect of silicon on activity coefficients of Bi, Cd, Sn, and Ag in liquid Fe-Si, and implications for differentiation and core formation. *Meteoritics & Planetary Science 54*, 1379-1394.

Rushmer, T., Minarik, W.G., and Taylor, G.J. (2000) Physical processes of core formation. *In Canup and Righter, eds., Origin of the Earth and Moon, University of Arizona Press, Tucson, AZ*, 227-243.

Sanloup, C., Jambon, A., and Gillet, P. (1999) A simple chondritic model of Mars. *Physics of the Earth and Planetary Interiors 112*, 43-54.

Sarbadhikari, A.B., Day, J.M., Liu, Y., Rumble III, D. and Taylor, L.A. (2009) Petrogenesis of olivine-phyric shergottite Larkman Nunatak 06319: Implications for enriched components in martian basalts. *Geochimica et Cosmochimica Acta 73*, 2190-2214.

Scheinberg, A., Elkins-Tanton, L. T., and Zhong, S. J. (2014) Timescale and morphology of Martian mantle overturn immediately following magma ocean solidification. *Journal of Geophysical Research: Planets 119*, 454-467.

Sharp, M., Righter, K., & Walker, R. J. (2015) Estimation of trace element concentrations in the lunar magma ocean using mineral-and metal-silicate melt partition coefficients. *Meteoritics & Planetary Science 50*, 733-758.

Shearer, C.K., McKay, G., Papike, J.J., & Karner, J.M. (2006) Valence state partitioning of vanadium between olivine-liquid: Estimates of the oxygen fugacity of Y980459 and application to other olivine-phyric martian basalts. *American Mineralogist 91*, 1657-1663.

Snyder, D.A. and Carmichael, I. S. (1992) Olivine-liquid equilibria and the chemical activities of FeO, NiO, Fe2O3, and MgO in natural basic melts. *Geochimica et Cosmochimica Acta 56* 303-318.

Stolper, E., Walker, D., Hager, B.H., and Hays, J.F. (1981) Melt segregation from partially molten source regions: the importance of melt density and source region size. *Journal of Geophysical Research: Solid Earth 86*(B7), 6261-6271.

Suzuki, T. and Akaogi, M. (1998) Element Partitioning Between Some Mantle Minerals and the Coexisting Silicate Melt Under High Pressure. In Properties of Earth and Planetary Materials at High Pressure and Temperature (eds M.H. Manghnani and T. Yagi). doi:10.1029/GM101p0261

Tait, K.T. and Day, J.M. (2018) Chondritic late accretion to Mars and the nature of shergottite reservoirs. *Earth and Planetary Science Letters 494*, 99-108.

Tonks, W.B. and Melosh, H.J. (1993) Magma ocean formation due to giant impacts. *Journal of Geophysical Research: Planets 98*(E3), 5319-5333.

van Westrenen, W. and Draper, D.S. (2007) Quantifying garnet-melt trace element partitioning using lattice-strain theory: new crystal-chemical and thermodynamic constraints. *Contributions to Mineralogy and Petrology 154*, 717-730.

Walker, R.J. (2009) Highly siderophile elements in the Earth, Moon and Mars: Update and implications for planetary accretion and differentiation. *Chemie der Erde* 69, 101-125.

Walker R. J., McDonough W. F., Honesto J., Chabot N. L., McCoy T. J., Ash R. D., and Bellucci J. J. (2008) Modeling fractional crystallization of group IVB iron meteorites. *Geochimica et Cosmochimica Acta* 72, 2198–2216.

Wasson J. T., Ouyang X., Wang J., and Jerde E. (1989) Chemical classification of iron meteorites: XI. Multielement studies of 38 new irons and the high abundance of ungrouped irons from Antarctica. *Geochimica et Cosmochimica Acta* 53, 735–744.

Walter, M.J., Nakamura, E., Trønnes, R.G., and Frost, D.J. (2004) Experimental constraints on crystallization differentiation in a deep magma ocean. *Geochimica et Cosmochimica Acta 68*, 4267-4284.

Wänke, H. and Dreibus, G. (1988) Chemical composition and accretion history of terrestrial planets. *Philosophical Transactions of the Royal Society of London. Series A, Mathematical and Physical Sciences 325*, 545-557.

Warren, P. H., Kallemeyn, G. W., and Kyte, F. T. (1999) Origin of planetary cores: evidence from highly siderophile elements in martian meteorites. *Geochimica et Cosmochimica Acta 63*, 2105-2122.

Yang, S., Humayun, M., Righter, K., Jefferson, G., Fields, D., and Irving, A.J. (2015) Siderophile and chalcophile element abundances in shergottites: Implications for Martian core formation. *Meteoritics & Planetary Science 50*, 691-714.

Yang, S., Humayun, M., and Salters, V. J. (2018) Elemental systematics in MORB glasses from the Mid-Atlantic Ridge. *Geochemistry, Geophysics, Geosystems 19*, 4236-4259.

Yang, S., Humayun, M., Righter, K., Irving, A. J., Hewins, R. H., and Zanda, B. (2020) Chalcophile Element Constraints on the Sulfur Content of the Martian Mantle. *51st Lunar Planet. Sci. Conf.,* #2326.

Yasuda, A., Fujii, T., and Kurita, K. (1994) Melting phase relations of an anhydrous mid-ocean ridge basalt from 3 to 20 GPa: Implications for the behavior of subducted oceanic crust in the mantle. *Journal of Geophysical Research: Solid Earth 99*(B5), 9401-9414.

Yurimoto, H. and Ohtani, E. (1992) Element partitioning between majorite and liquid: a secondary ion mass spectrometric study. *Geophysical Research Letters 19*, 17-20.

Zhang, J., & Herzberg, C. (1994) Melting experiments on anhydrous peridotite KLB-1 from 5.0 to 22.5 GPa. *Journal of Geophysical Research: Solid Earth 99*(B9), 17729-17742.

Figure Captions

Figure 1: Stages in differentiation of Mars, including a) the early magma ocean to a pressure of ~ 14 GPa as suggested by siderophile element partitioning (Righter and Chabot, 2011; Rai and van Westrenen, 2013; Righter et al., 2015; Yang et al., 2015); b) crystallization of the magma ocean from nearly complete melting to low melt fraction (shown here schematically as 1%); c) trapping of residual liquid in the solid mantle at the end of magma ocean crystallization; and d) later melting of the heterogeneous mantle that is comprised of enriched and depleted portions created by the magma ocean crystallization.

Figure 2a: Correlations between lithophile isotope system εNd and the Os isotopic system (γ Os) for martian meteorites, thought to be a result of early differentiation processes in the martian mantle (data from Brandon et al., 2012 and references therein). **Figure 2b:** Crystallization-age corrected Sr versus Os isotope compositions for martian shergottite meteorites (data from Tait and Day, 2018, and references therein). Models to explain these trends between Os-Sr-Nd isotopic values are currently hindered by lack of partitioning data for high pressure phases relevant to the deep martian mantle.

Figure 3: Back scattered electron images of experimental run products from this study. A) Experiment #208, showing large garnet crystals and co-existing melt, along with analytical spots and tracks from the LA-ICP-MS analysis (100 μm scale bar). B) higher magnification image of a garnet-melt pair from experiment #207 (10 μm scale bar). C) Experiment #207, showing large olivine crystals and co-existing melt, along with analytical spots and tracks from the LA-ICP-MS analysis (100 μm scale bar). D) higher magnification image of an olivine-melt pair from experiment #207 (10 μm scale bar). E) garnet-olivine-melt run product from experiment #258, with dark areas being the graphite capsule material (100 μm

scale bar). F) Enlarged image of the garnet and olivine portions of the run product from experiment #258 (50 μm scale bar). G) image of entire run product of experiment #266 showing two triangular regions consisting of wadsleyite and melt (100 μm scale bar). H) Close-up image of a wadsleyite-melt pair from experiment 266 (10 μm scale bar). I) image of entire run product of experiment #368 showing large wadsleyite crystals and melt regions (100 μm scale bar). J) Close-up image of a wadsleyite-melt region from experiment 368 (10 μm scale bar). In all experiments (and images), silicate melt regions did not quench to a glass, but rather fine-grained polyphase crystals.

Figure 4: Comparison of our partitioning results with several selected literature results A) Sc, V, Ga, and Cr D(majorite/melt) (with comparison to results from Righter and Drake, 2000; Yurimoto and Ohtani, 1992; Corgne et al. 2012; and van Westrenen and Draper, 2003). B) D(Ru) olivine/melt and wadsleyite/melt from our study compared to olivine/melt results reported by Brenan et al. (2003), Righter et al. (2004), and Sharp et al. (2015).

Figure 5: Demonstration of fractionation of several HSE ratios – Re/Os, Pd/Ir, and Pt/Os – by garnet and olivine removal, calculated using the results of experiments 207 and 208. Because the HSE are largely incompatible in olivine, these ratios are not significantly fractionated during olivine removal from (or addition to) the system. Garnet shows slightly greater potential for fractionating Re/Os, Pd/Ir, and Pt/Os, but only the latter is significant with 5% change after 20% fractionation.

Figure 6: Calculated HSE content of the martian mantle after core formation. Comparison is made to the terrestrial mantle. Also calculated are liquids and solids after 80% (20% liquid) and 99% crystallized (1% liquid). Note that the Re, Au, Pd, and Ru contents all increase by

5-20x during crystallization, whereas Os, Pt, and Ir all increase by a smaller amount. This will lead to portions of the mantle with higher Re/Os and Pd/Ir ratios, for example.

Figure 7: Fractionation of Re-Os, Rb-Sr, Sm-Nd, and Lu-Hf during crystallization of a magma ocean, using shallow and deep mantle phases. The calculations for shallow crystallization used the D(Re) and D(Os) values determined for experiment 208, and for deep crystallization used experiment 258 for the deep conditions; a deep magma ocean will be convecting and thus minerals crystallizing over a wider pressure range (Table 3), and thus the average of shallow and deep was used for modelling deep magma ocean crystallization.

Figure 8: Evolution of $^{187}Re/^{188}Os$ and $^{147}Sm/^{144}Nd$ of modelled liquids and solids during equilibrium crystallization of a martian magma ocean, using partition coefficients from Table 3 and for the deep melting and crystallization scenarios of Figure 7. For comparison are the $^{187}Re/^{188}Os$ and $^{147}Sm/^{144}Nd$ of shergottites from Brandon et al. (2012). The shergottites can be explained by mixing of liquids with cumulate solids across a range of ratios between 25:75 and 45:55 (liquid:solid).

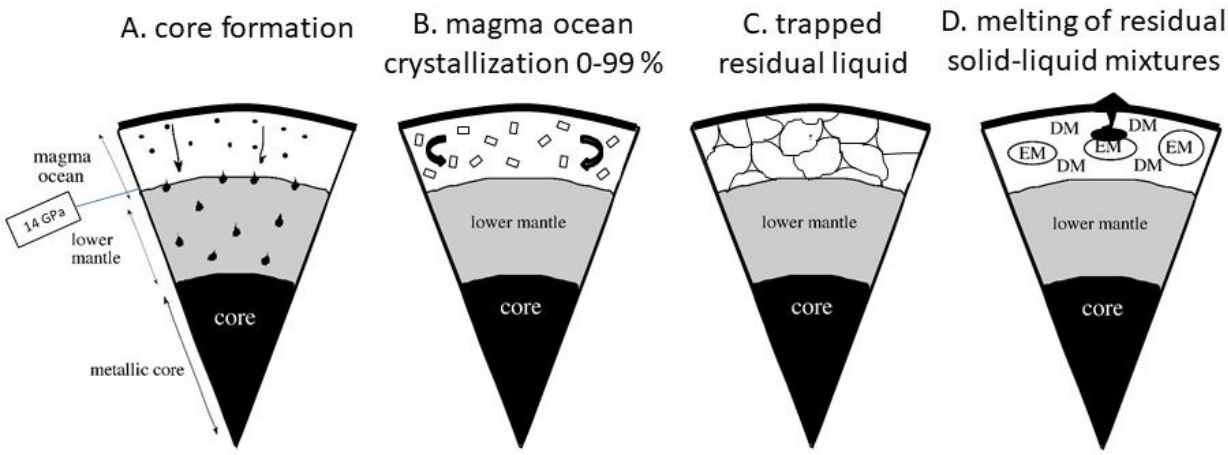
A. core formation
B. magma ocean crystallization 0-99 %
C. trapped residual liquid
D. melting of residual solid-liquid mixtures
magma ocean
14 GPa
lower mantle
core
metallic core
lower mantle
core
lower mantle
core
DM
EM
DM
EM
DM
EM
DM
lower mantle
core

Figure 1

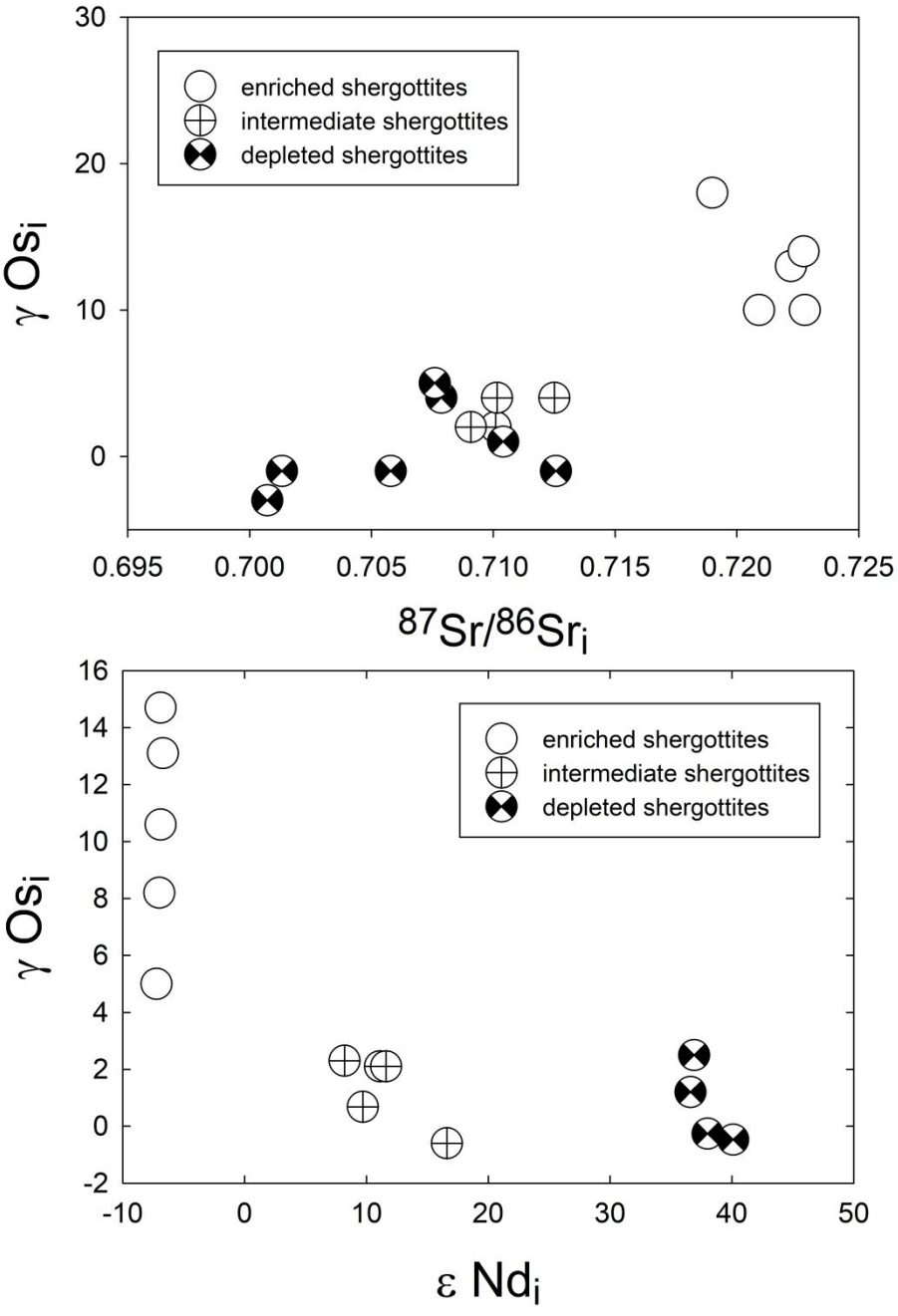
enriched shergottites
intermediate shergottites
depleted shergottites
γ Os$_i$
^{87}Sr/^{86}Sr$_i$
ε Nd$_i$

Figure 2

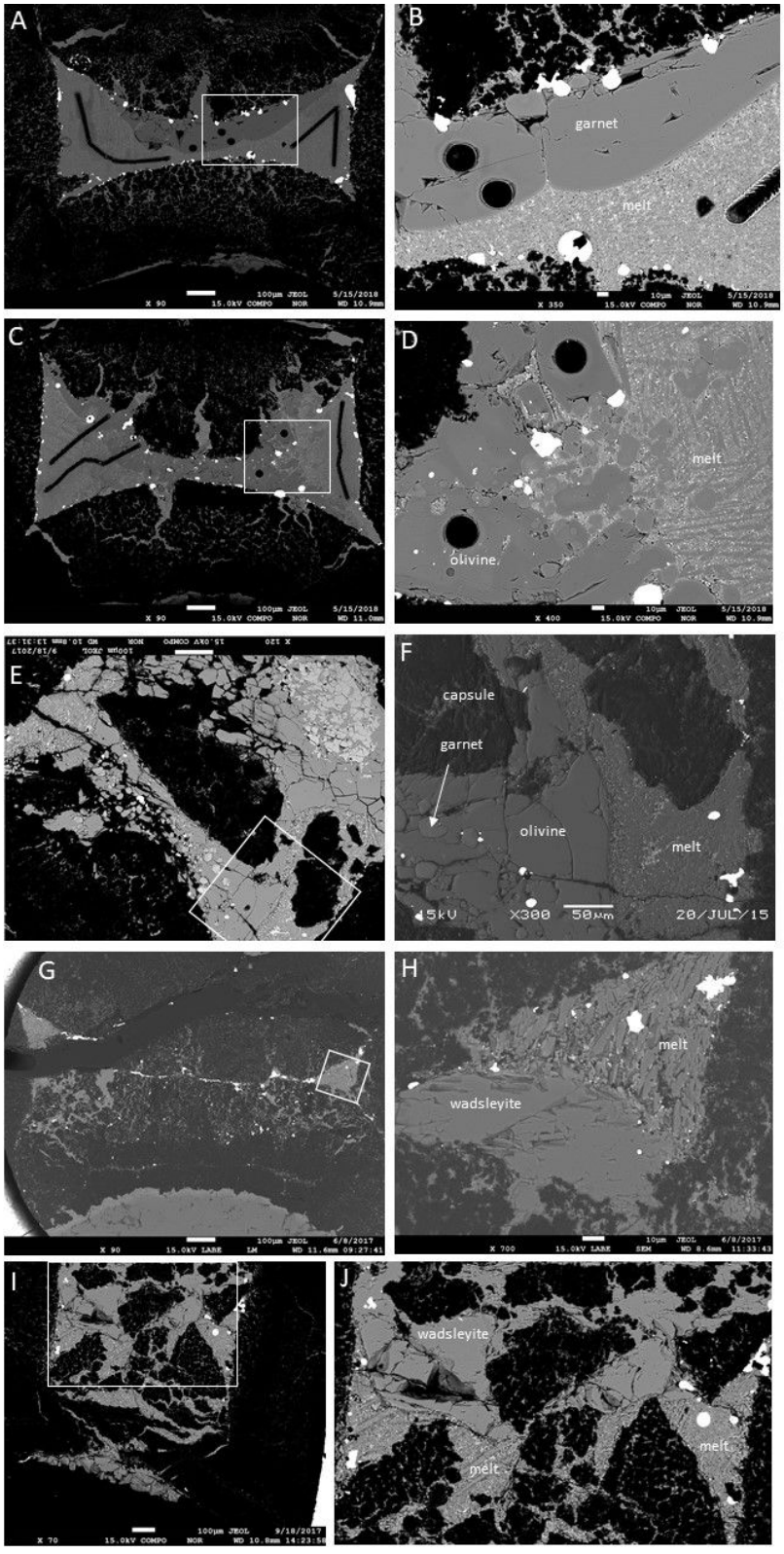
A
B
garnet
melt
C
D
melt
olivine
E
F
capsule
garnet
olivine
melt
5kV X300 50µm 20/JUL/15
G
H
melt
wadsleyite
I
J
wadsleyite
melt
melt

Figure 3

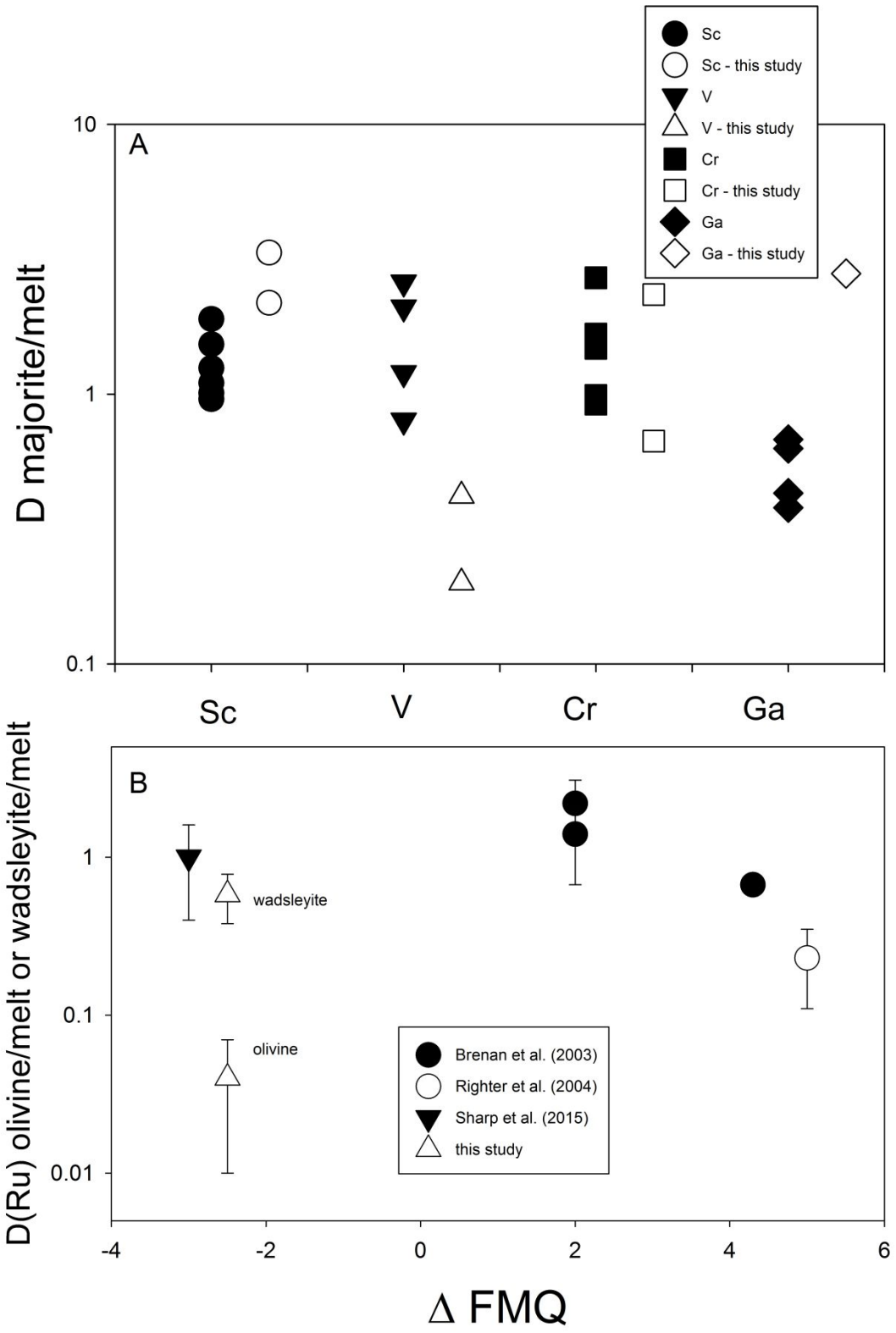
A
B
Sc
Sc - this study
V
V - this study
Cr
Cr - this study
Ga
Ga - this study
D majorite/melt
10
1
0.1
Sc
V
Cr
Ga
D(Ru) olivine/melt or wadsleyite/melt
wadsleyite
olivine
Brenan et al. (2003)
Righter et al. (2004)
Sharp et al. (2015)
this study
0.01
-4
-2
0
2
4
6
Δ FMQ

Figure 4

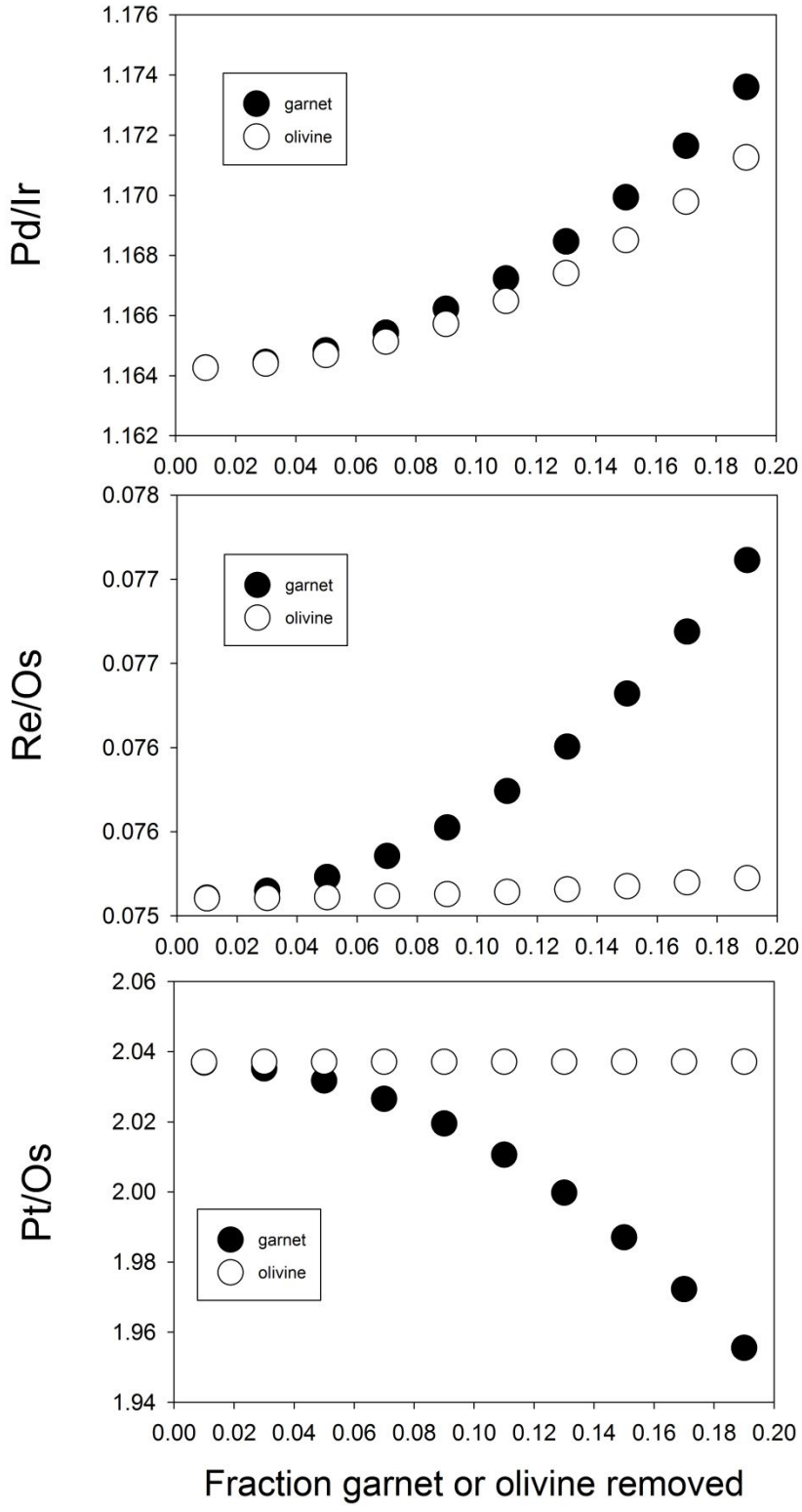
Pd/Ir
1.176
1.174
1.172
1.170
1.168
1.166
1.164
1.162
garnet
olivine
0.00 0.02 0.04 0.06 0.08 0.10 0.12 0.14 0.16 0.18 0.20
Re/Os
0.078
0.077
0.077
0.076
0.076
0.075
garnet
olivine
0.00 0.02 0.04 0.06 0.08 0.10 0.12 0.14 0.16 0.18 0.20
Pt/Os
2.06
2.04
2.02
2.00
1.98
1.96
1.94
garnet
olivine
0.00 0.02 0.04 0.06 0.08 0.10 0.12 0.14 0.16 0.18 0.20
Fraction garnet or olivine removed

Figure 5:

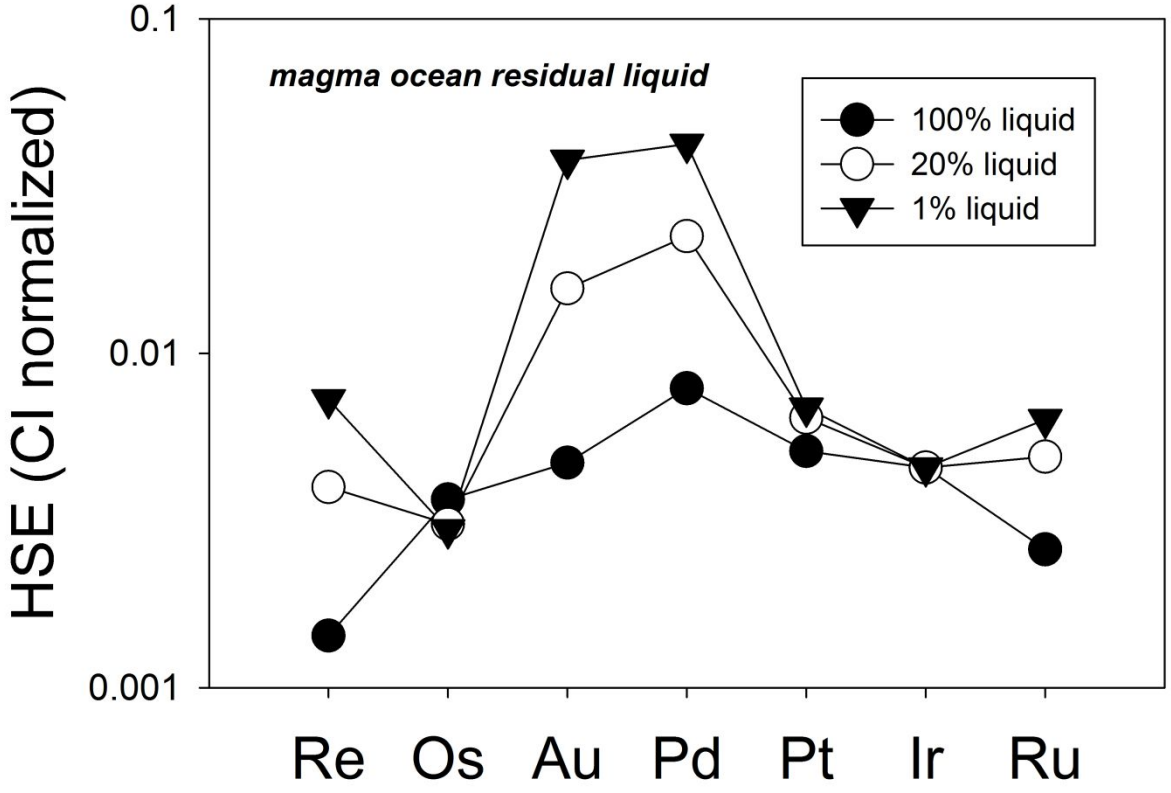
magma ocean residual liquid
100% liquid
20% liquid
1% liquid
HSE (CI normalized)
0.1
0.01
0.001
Re
Os
Au
Pd
Pt
Ir
Ru

Figure 6

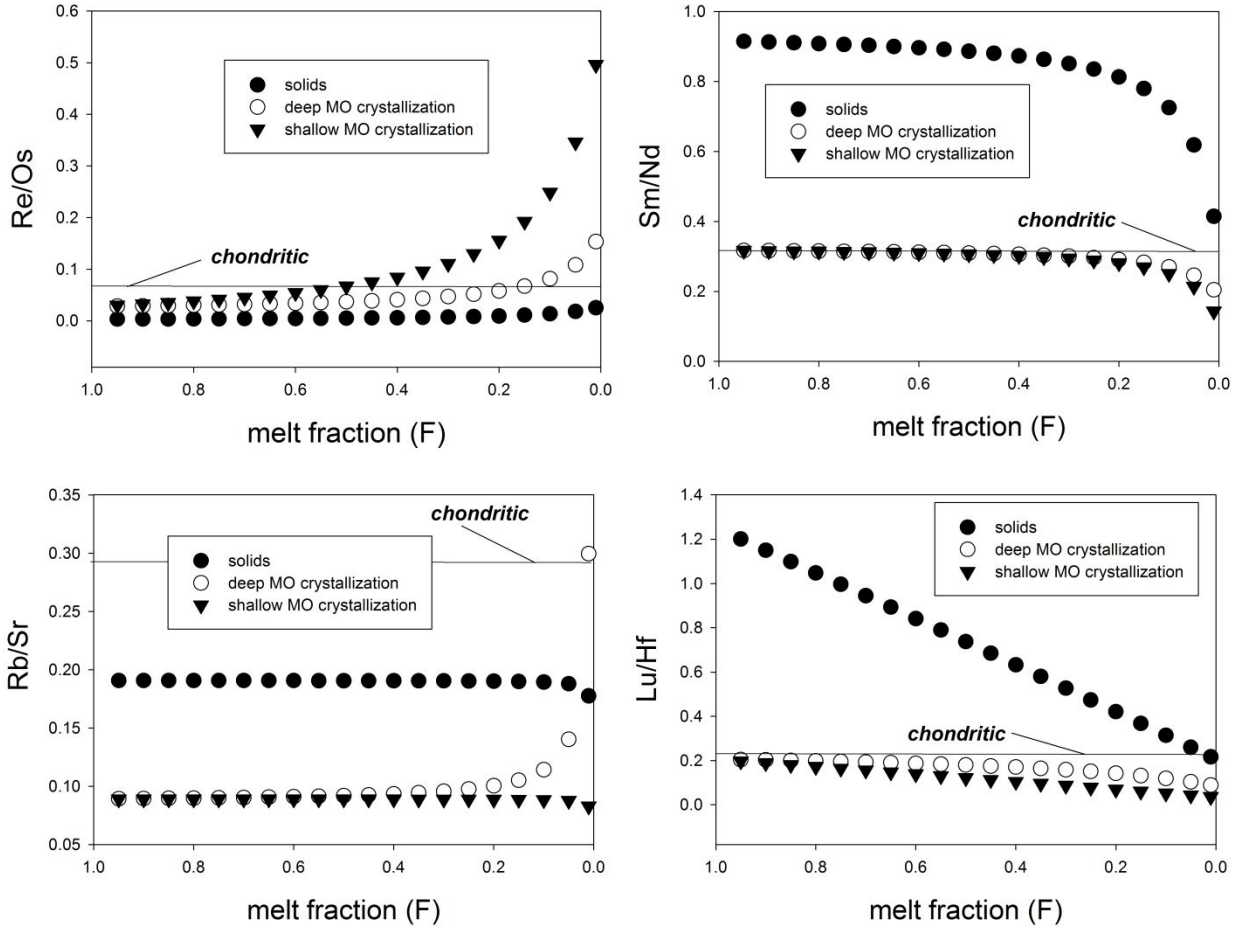
Re/Os
Sm/Nd
Rb/Sr
Lu/Hf
solids
deep MO crystallization
shallow MO crystallization
chondritic
melt fraction (F)

Figure 7

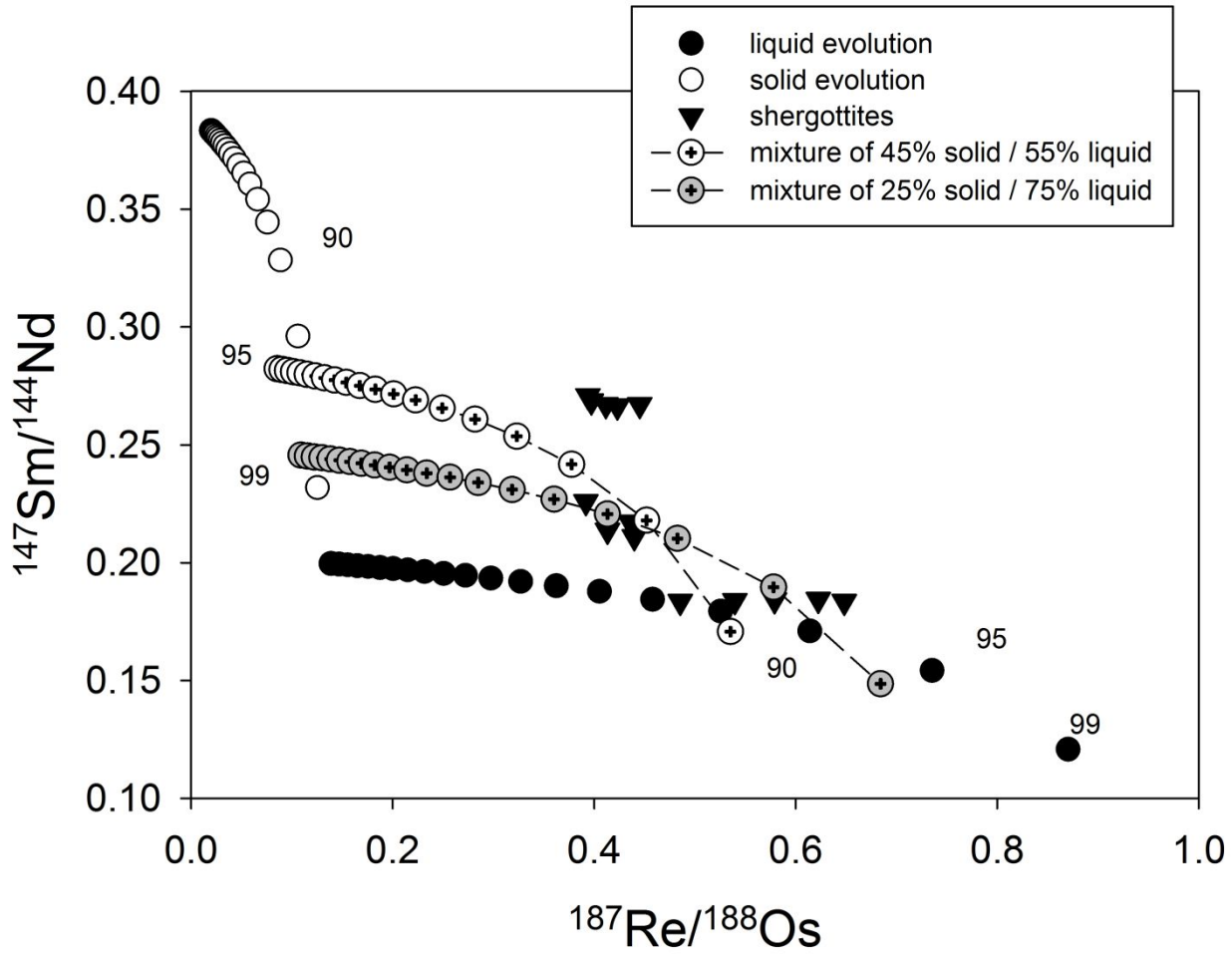
liquid evolution
solid evolution
shergottites
mixture of 45% solid / 55% liquid
mixture of 25% solid / 75% liquid
0.40
0.35
0.30
0.25
0.20
0.15
0.10
0.0
0.2
0.4
0.6
0.8
1.0
147Sm/144Nd
187Re/188Os
90
95
99
90
95
99

Figure 8

Table 1: Run conditions

Exp#	P (GPa)	T (°C)	Duration (min)	Result
207	13	1730	10	oliv, liq
208	14	1730	10	garnet, liq
258	15	1770	35	garnet, oliv, liq
266	15	1770	10	wadsleyite, liq
368	17	1880	30	wadsleyite. liq

Table 2: Electron microprobe and laser ablation analyses of crystals and quenched liquids

	208				**207**				**258**						**266**				**368**		
Wt% EMPA	Grt	melt	**D (gt/ melt)**		oliv	melt	**D (oliv/ melt)**		Grt*	oliv	melt	**D (Grt/ melt)**	**D (oliv/m elt)**		wadsl	melt	**D (wadsl /melt)**		wadsl	melt	**D (wadsl/m elt)**
SiO_2	59.3	45.9	**1.29**		41.83	42.85	**0.98**		48.1	40	25	**1.91**	**1.59**		40.21	35.86	**1.12**		43.18	29.73	**1.452**
TiO_2	0.01	0.12	**0.1**		0.001	0.13	**0.005**		0.008	-	0.173	**0.049**	**-**		-	0.12	**-**		-	0.16	**-**
Al_2O_3	1.12	2.08	**0.54**		0.51	3.04	**0.17**		14.7	0.21	2.3	**6.25**	**0.089**		0.14	2.52	**0.054**		0.12	2.12	**0.054**
Cr_2O_3	0.33	0.5	**0.67**		0.25	0.76	**0.32**		1.5	0.09	0.62	**2.34**	**0.15**		0.091	0.58	**0.16**		0.09	0.5	**0.171**
FeO_T	6.69	15.8	**0.42**		7.43	14.04	**0.53**		9.6	5.2	13	**0.74**	**0.4**		5.33	12.96	**0.41**		4.16	10.11	**0.412**
MnO	0.25	0.56	**0.44**		0.19	0.47	**0.41**		0.4	0.1	0.44	**1.02**	**0.23**		0.098	0.32	**0.31**		0.11	0.44	**0.241**
MgO	31.2	31.8	**0.98**		49.62	33.9	**1.46**		23.3	54	52	**0.45**	**1.03**		53.77	44.05	**1.22**		52.13	50.39	**1.034**
CaO	0.53	2.09	**0.25**		0.09	2.7	**0.03**		0.9	0.15	3.66	**0.25**	**0.04**		0.073	2.1	**0.035**		0.06	3.38	**0.018**
Na_2O	0.54	1.21	**0.44**		0.09	2.13	**0.04**		0.63	0.45	1.6	**0.41**	**0.29**		0.16	0.57	**0.29**		0.08	1.67	**0.048**
K_2O	-	-	**-**		-	-	**-**		0.4	0.16	0.2	**2.12**	**0.81**		0.049	0.043	**1.14**		-	-	**-**
P_2O_5	-	-	**-**		-	-	**-**		0.32	0.03	0.9	**0.35**	**0.03**		0.079	0.87	**0.09**		0.07	1.43	**0.049**
(ppm)	LA-ICP-MS																				
B	-	-	**-**		-	-	**-**		-	6	54	**-**	**0.11**		10	35	**0.30**		4	64	**0.061**
S	-	-	**-**		-	-	**-**		0.05	-	0.01	**3.5**	**-**		0.03	0.03	**1.0**		0.002	0.03	**0.08**
Sc	2.2	1.0	**2.2**		0.03	2.0	**0.02**		15	5.6	4.5	**3.4**	**1.2**		1.8	2.0	**0.9**		3.0	6.5	**0.5**
V	1.9	10	**0.19**		1.0	13	**0.08**		6.7	1	16	**0.42**	**0.06**		0.59	10	**0.06**		0.6	12	**0.05**
Co	14	23	**0.6**		19	20	**0.94**		9.2	14	16	**0.59**	**0.87**		13	17	**0.757**		4.21	3.54	**1.19**
Ni	23	36	**0.6**		18	43	**0.4**		47	72	47	**1.0**	**1.5**		168	206	**0.8**		10	1.4	**7.6**
Cu	-	-	**-**		-	-	**-**		3	8	41	**0.06**	**0.2**		22	22	**1.0**		4	39	**0.1**
Zn	-	-	**-**		-	-	**-**		4.4	9.4	26	**0.17**	**0.36**		19	33	**0.56**		10	27	**0.39**
Ga	-	-	**-**		-	-	**-**		1.3	0.17	0.5	**2.8**	**0.36**		0.47	0.34	**1.38**		0.18	1.54	**0.11**
Ge	-	-	**-**		-	-	**-**		-	-	-	**-**	**-**		-	0.1	**-**		0.3	0.7	**0.5**
Sr	-	-	**-**		-	-	**-**		1.29	0.98	27	**0.047**	**0.036**		0.47	17	**0.027**		-	46	**-**

Y	-	-	**-**		-	-	**-**		0.66	-	23	**0.029**	**-**		0.25	13	**0.019**		0.09	61	**0.0014**
Zr	-	-	**-**		-	-	**-**		9.27	0.14	332	**0.028**	**0.0004**		1.59	53	**0.03**		0.39	1120	**0.00035**
Nb	0.05	0.4	**0.12**		0.02	0.62	**0.03**		-	0.03	1.33	**-**	**0.019**		-	0.46	**-**		0.04	43	**0.00098**
Mo	0.9	14	**0.07**		0.4	78	**0.01**		4.2	4.5	268	**0.016**	**0.017**		-	116	**-**		-	75	**-**
W	0.71	10.6	**0.07**		2.68	1590	**0**		61	0.67	5240	**0.012**	**0.00013**		2.63	35	**0.075**		0.41	6040	**0.00007**
Ru	0.4	3.0	**0.14**		0.08	2.5	**0.03**		83*	0.5	3.3	**25***	**0.13**		11	18	**0.6**		-	9	**-**
Rh	0.8	3.1	**0.25**		0.2	3.5	**0.07**		17*	0.17	2.5	**6.9***	**0.068**		23	81	**0.29**		-	6.3	**-**
Pd	8.7	87	**0.1**		1.6	75	**0.02**		80*	1.05	99	**0.8***	**0.01**		123	303	**0.4**		-	6.9	**-**
Ba	-	-	**-**		-	-	**-**		7.49	0.71	1677	**0.004**	**0.00042**		16.2	1129	**0.014**		-	4569	**-**
La	-	-	**-**		-	-	**-**		84	0.68	19700	**0.004**	**0.00003**		3.7	129	**0.029**		-	3387	**-**
Re	27	245	**0.11**		3.5	243	**0.01**		320	5.3	1020	**0.32**	**0.005**		590	3030	**0.20**		5	333	**0.016**
Os	1.64	2.17	**0.76**		<0.02	0.31	**<0.05**		335*	0.13	0.06	**5970***	**2.4**		42	128	**0.328**		-	2.4	**-**
Ir	0.027	0.09	**0.3**		<0.01	0.08	**<0.17**		-	-	0.03	**-**	**-**		2.5	0.71	**3.57**		0.07	0.45	**0.16**
Pt	5.2	2.9	**1.8**		<0.02	0.4	**<0.04**		76*	0.04	0.3	**240***	**0.13**		35	349	**0.1**		-	0.23	**-**
Au	1.5	16	**0.09**		0.07	14	**0.01**		30*	-	13	**2.3***	**-**		40	320	**0.13**		-	12	**-**
Pb	-	-	-		-	-	-		-	0.06	3.53	-	0.017		0.072	0.63	0.12		-	21	-
Th	-	-	-		-	-	-		-	-	0.39	-	-		-	0.18	-		-	8.3	-
U	-	-	-		-	-	-		-	-	0.69	-	-		-	0.37	-		-	6.0	-

(* - affected by HSE nugget and D for Ru, Rh, Pd, Os, Pt, Au)
"-" indicates no data or below detection limit.

Table 3: Summary of partition coefficients from this study and those used in modelling (see text)

	oliv	cpx	gt	**shallow**	majorite	cpx	wads	**deep**	**mix/average**	Brandon et al. 2012
%	65	10	25		35	5	60			
D Re	0.03	0.2	0.50	**0.16**	0.2	0.2	0.2	**0.20**	**0.18**	1.2
D Os	2.75	0.4	0.76	**2.02**	0.76	0.4	0.33	**0.48**	**1.25**	7.9
D Pd	0.02	0.05	0.1	**0.04**	0.1	0.05	0.41	**0.28**	**0.16**	
D Pt	0.04	1.5	1.78	**0.62**	1.78	1.5	0.1	**0.76**	**0.69**	
D Ru	0.08	2	0.14	**0.28**	0.14	2	0.58	**0.50**	**0.39**	
D Au	0.12	0.05	0.09	**0.11**	0.09	0.05	0.13	**0.11**	**0.11**	
D Sm	0.001	0.17	0.1	**0.063**	0.1	0.17	3E-05	**0.052**	**0.058**	
D Nd	0.001	0.11	0.04	**0.037**	0.04	0.107	3E-05	**0.018**	**0.027**	0.025
D Rb	0.001	0.011	0.001	**0.0036**	0.001	0.011	0.002	**0.0015**	**0.0025**	
D Sr	0.001	0.12	0.001	**0.036**	0.001	0.12	0.0003	**0.0007**	**0.018**	
D Lu	0.001	0.28	1.93	**0.28**	1.93	0.28	0.002	**0.97**	**0.63**	
D Hf	0.001	0.23	0.32	**0.11**	0.32	0.233	0.002	**0.16**	**0.14**	

Sources: D(Re, Os, Pd, Pt, Ru) oliv/melt, cpx/melt, and garnet/melt from Mallmann and O'Neill (2007), Sharp et al. (2015) and references therein; other mineral/melt D from studies of Draper et al. (2003), Corgne et al. (2012), Yurimoto and Ohtani (1992) and Mibe et al. (2006).

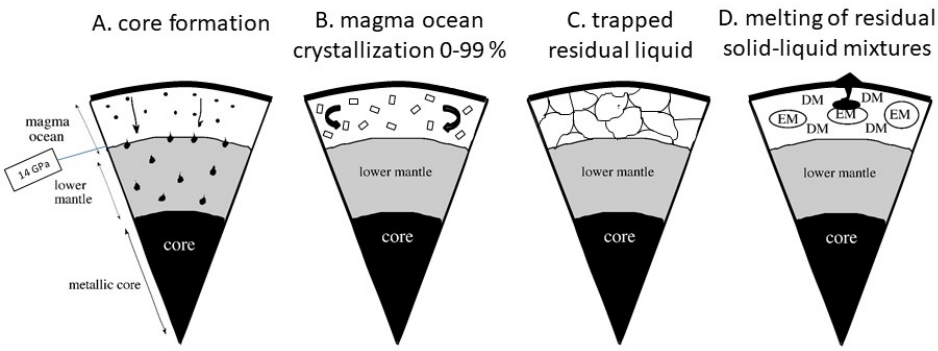

Figure 1

254x190mm (96 x 96 DPI)

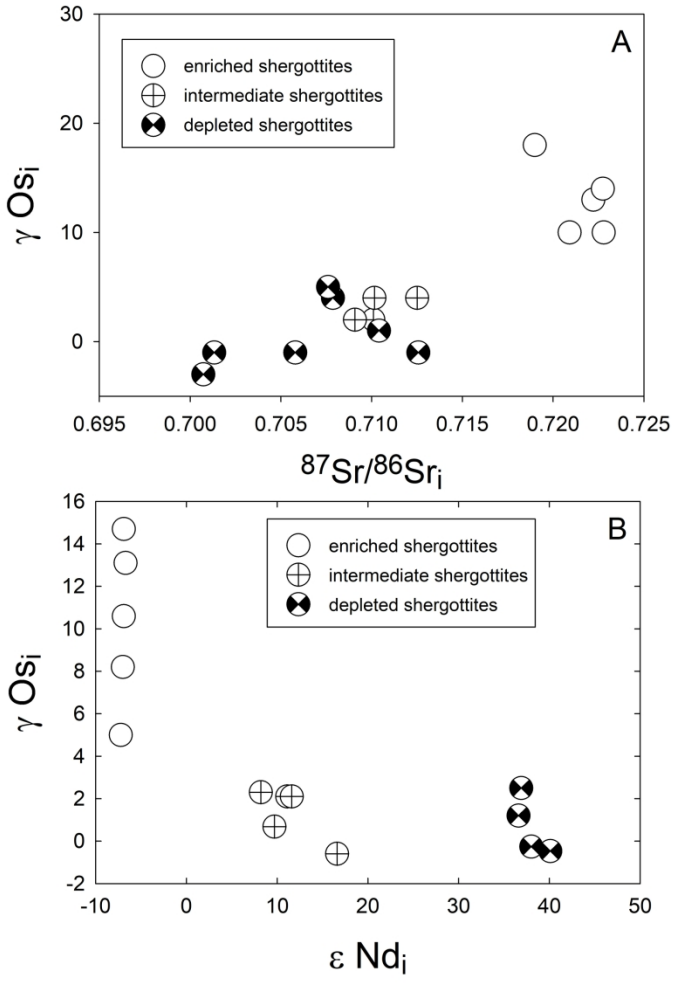

Figure 2

215x279mm (300 x 300 DPI)

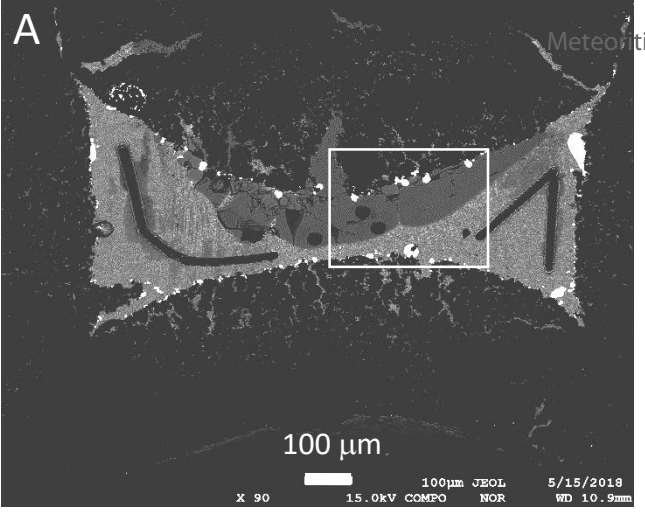
A
100 µm
100µm JEOL 5/15/2018
X 90 15.0kV COMPO NOR WD 10.9mm

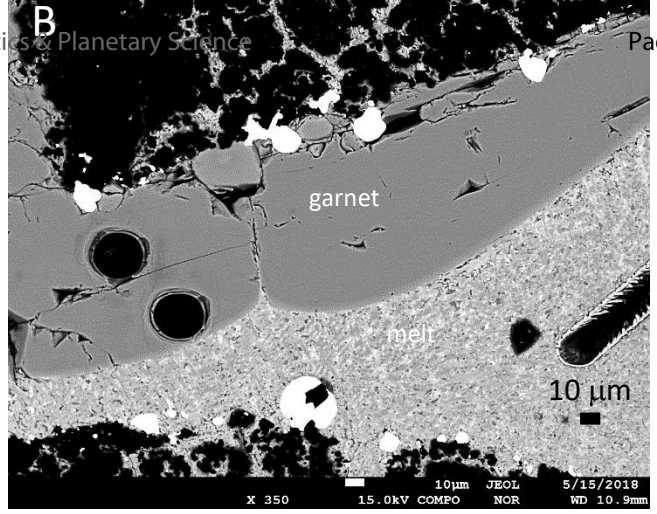
B
garnet
melt
10 µm
10µm JEOL 5/15/2018
X 350 15.0kV COMPO NOR WD 10.9mm

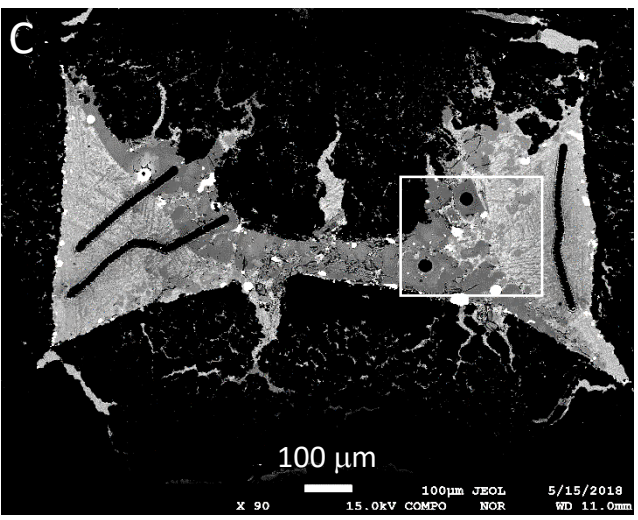
C
100 µm
100µm JEOL 5/15/2018
X 90 15.0kV COMPO NOR WD 11.0mm

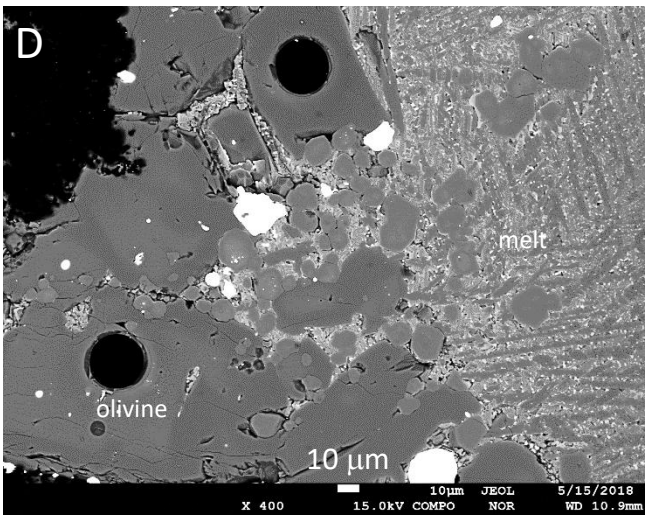
D
melt
olivine
10 µm
10µm JEOL 5/15/2018
X 400 15.0kV COMPO NOR WD 10.9mm

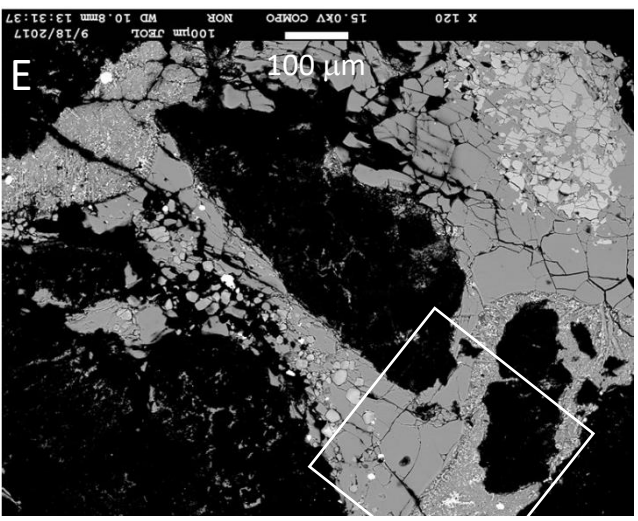
E
100 µm

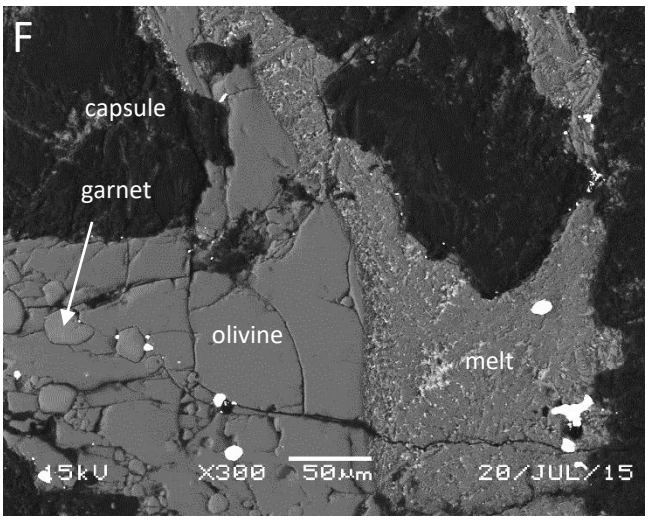
F
capsule
garnet
olivine
melt
15kV X300 50µm 20/JULY/15

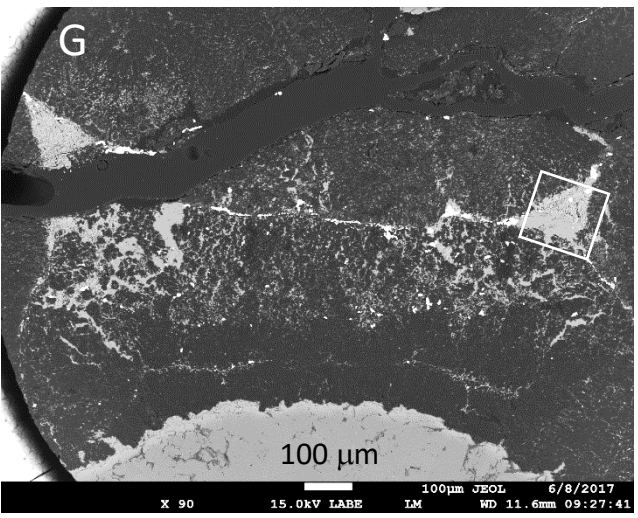
G
100 µm
100µm JEOL 6/8/2017
X 90 15.0kV LABE LM WD 11.6mm 09:27:41

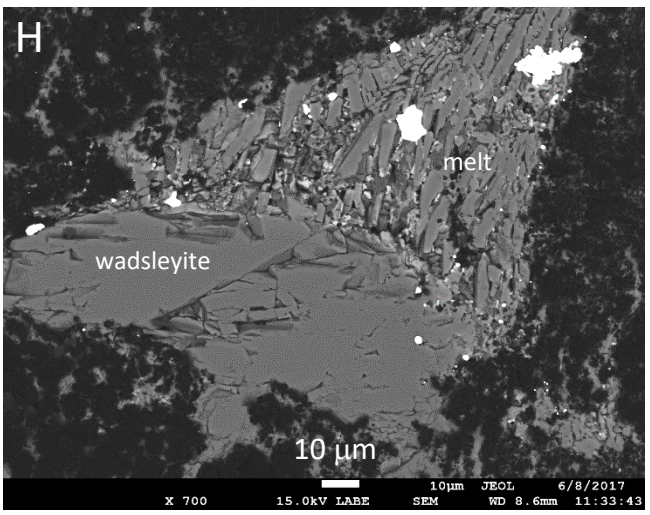
H
melt
wadsleyite
10 µm
10µm JEOL 6/8/2017
X 700 15.0kV LABE SEM WD 8.6mm 11:33:43

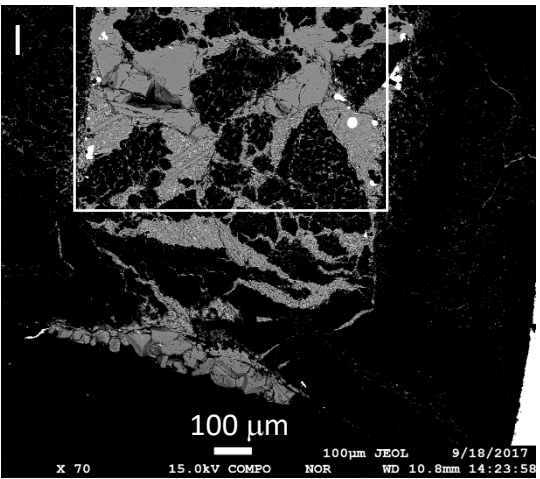
I
100 µm
100µm JEOL 9/18/2017
X 70 15.0kV COMPO NOR WD 10.8mm 14:23:58

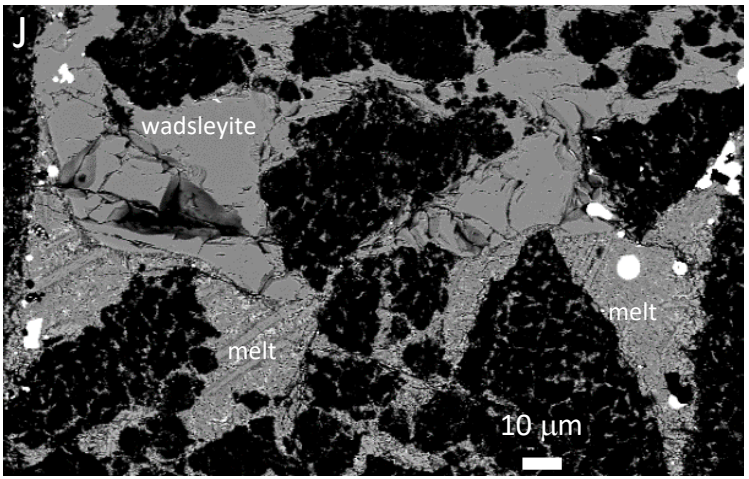
J
wadsleyite
melt
melt
10 µm

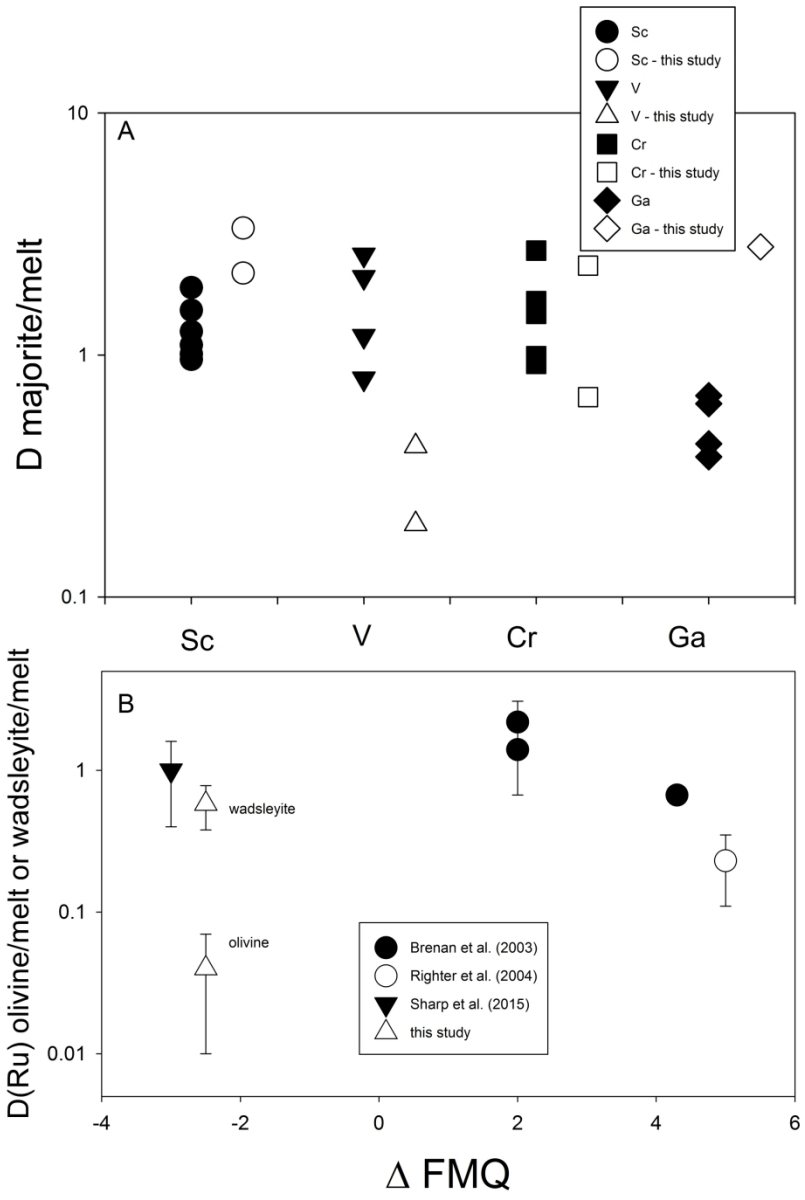

Figure 4

215x292mm (300 x 300 DPI)

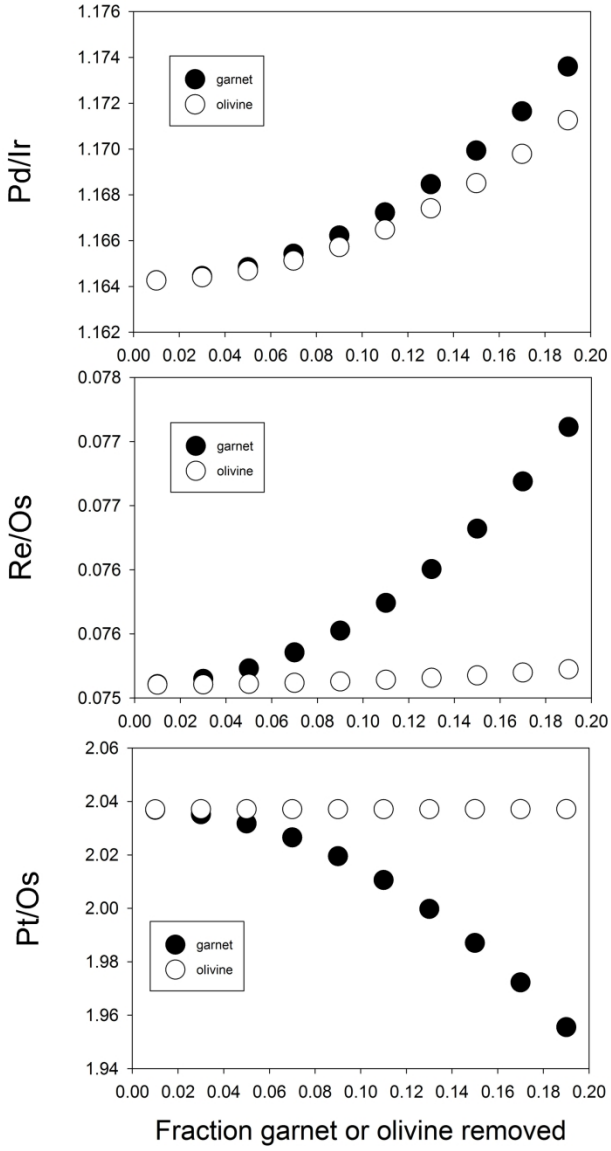

Figure 5

215x279mm (300 x 300 DPI)

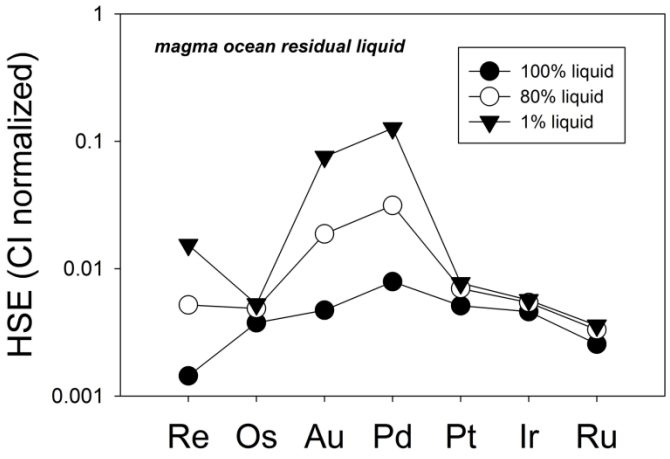

Figure 6

215x279mm (300 x 300 DPI)

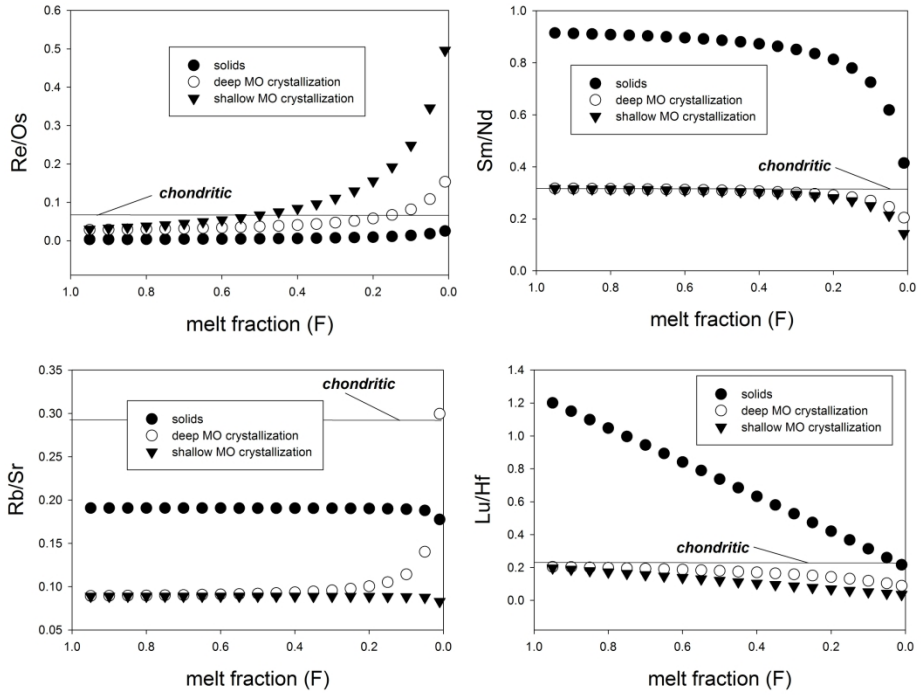

Figure 7

215x279mm (300 x 300 DPI)

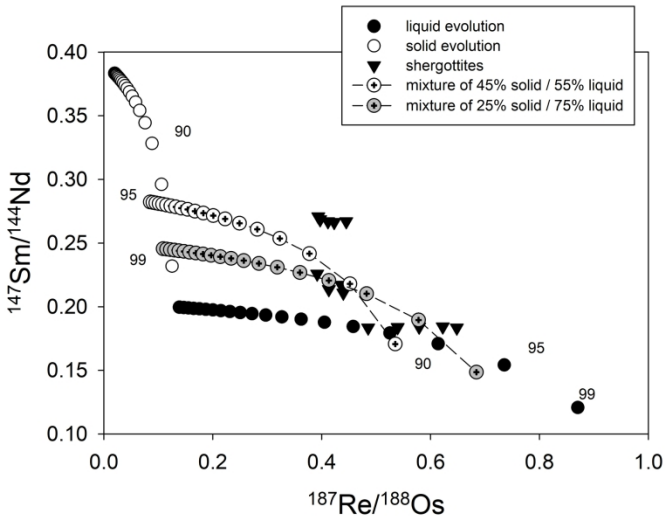

Figure 8

215x279mm (300 x 300 DPI)